The Astrophysical Journal, 699:453–468, 2009 July 1 doi:10.1088/0004-637X/699/1/453

DETERMINATION OF BLACK HOLE MASSES IN GALACTIC BLACK HOLE BINARIES USING SCALING OF SPECTRAL AND VARIABILITY CHARACTERISTICS

Nickolai Shaposhnikov[1,2] and Lev Titarchuk[3,4,5,6,7]
[1] Department of Astronomy, CRESST/University of Maryland, College Park, MD 20742, USA; nikolai.v.shaposhnikov@nasa.gov
[2] Goddard Space Flight Center, NASA, Astrophysics Science Division, code 662, Greenbelt, MD 20771, USA
[3] George Mason University/Center for Earth Observing and Space Research, Fairfax, VA 22030, USA
[4] US Naval Research Laboratory, Code 7655, Washington, DC 20375-5352, USA; lev.titarchuk@nrl.navy.mil
[5] Goddard Space Flight Center, NASA, Code 661, Greenbelt, MD 20771, USA; lev@milkyway.gsfc.nasa.gov
[6] Dipartimento di Fisica, Università di Ferrara, Via Saragat 1, 1-44100 Ferrara, Italy
[7] ICRANet, Piazza della Repubblica 10 65122 Pescara (PE), Italy
Received 2008 February 1; accepted 2009 March 4; published 2009 June 12

ABSTRACT

We present a study of correlations between X-ray spectral and timing properties observed from a number of Galactic black hole (BH) binaries during hard–soft state spectral evolution. We analyze 17 transition episodes from eight BH sources observed with *Rossi X-Ray Timing Explorer*. Our scaling technique for BH mass determination uses a correlation between the spectral index and quasi-periodic oscillation (QPO) frequency. In addition, we use a correlation between the index and the normalization of the disk "seed" component to cross-check the BH mass determination and estimate the distance to the source. While the index–QPO correlations for two given sources contain information on the ratio of the BH masses in those sources, the index–normalization correlations depend on the ratio of the BH masses and the distance square ratio. In fact, the index–normalization correlation also discloses the index–mass accretion rate saturation effect given that the normalization of disk "seed" photon supply is proportional to the disk mass accretion rate. We present arguments that this observationally established index saturation effect is a signature of the bulk motion (converging) flow onto a BH, which was early predicted by the dynamical Comptonization theory. We use GRO J1655−40 as a primary reference source for which the BH mass, distance, and inclination angle are evaluated by dynamical measurements with unprecedented precision among other Galactic BH sources. We apply our scaling technique to determine BH masses and distances for Cygnus X-1, GX 339−4, 4U 1543−47, XTE J1550−564, XTE J1650−500, H 1743−322, and XTE J1859−226. A good agreement of our results for sources with known values of BH masses and distance provides independent verification for our scaling technique.

Key words: accretion, accretion disks – black hole physics – radiation mechanisms: non-thermal – stars: individual (XTE J1550−564, H 1743−322, GX 339−4, 4U 1630−47, GRS 1915+105, XTE 1650−500, XTE 1859+226, 4U 1543−47)

Online-only material: machine-readable table, color figures

1. INTRODUCTION

Determination of masses of Galactic black holes (BHs) is one of the most important tasks in modern astronomy. In general, knowledge of the BH mass distribution of the Galaxy can provide important clues on stellar evolution. It can also constrain the maximum mass of a neutron star and the minimum mass of a BH. For example, Rhoades & Ruffini (1974) predicted that the maximum mass of a neutron star, formed as a result of a supernova explosion, is probably about 3.2 solar masses. The study of the characteristic changes in spectral and variability properties of X-ray binaries (XRBs) proved to be a valuable source of information on the physics governing the accretion processes and on the fundamental parameters of BHs.

BH observational appearance is conventionally described in terms of BH state classification (see Remillard & McClintock 2006; Belloni 2005; Klein-Wolt & van der Klis 2008, for different flavors of BH state definitions). We adopt the following general BH state classification for five major BH states: *quiescent*, *low-hard* (LHS), *intermediate* (IS), *high-soft* (HSS), and *very high* states (VHS). When a BH transient goes into outburst it leaves a quiescent state and enters the LHS, a low-luminosity state with the energy spectrum dominated by a Comptonization component combined (convolved) with a weak thermal component. The photon spectrum in the LHS is presumably a result of Comptonization (upscattering) of soft photons, which originated in a relatively weak accretion disk, off electrons of the hot ambient plasma (see, e.g., Sunyaev & Titarchuk 1980). Variability in the LHS is high (fractional rms variability is up to 40%) and presented by a flat-top broken power-law (white–red noise) shape, accompanied by quasi-periodic oscillations (QPOs) in the range of 0.01–30 Hz, observed as narrow peaks in the power density spectrum (PDS). The HSS photon spectrum is characterized by a prominent thermal component, which is probably a signature of a strong emission coming from a geometrically thin accretion disk. A weak power-law component is also present at the level of not more than 20% of the total source flux. In the HSS, the flat-top variability ceases, QPOs disappear, and the PDS acquires a pure power-law shape. The total variability in the HSS is usually about 5% fractional rms. The IS is a transitional stage between the LHS and HSS.

The timing and spectral properties of an accreting BH are tightly correlated (see a comprehensive set of references in Table 1). Correlations between the spectral hardness (photon index) and the characteristic frequencies of the quasi-periodic variability observed in the light curves of BH sources have been

Table 1
Spectral Transition Data Used in Analysis

Source	Transition ID	Start	End	Type	Refs.
GRO J1655−40	J1655−R05	22/02/05	13/03/05	Rise	11
	J1655−D05	11/09/05	27/09/05	Decay	11
GX 339−4	GX339−R02	23/04/02	18/05/02	Rise	4, 5
	GX339−D03	20/02/03	05/06/03	Decay	
	GX339−R04	10/07/04	20/08/04	Rise	
	GX339−R07	22/01/07	18/02/07	Rise	
	GX339−D07	07/05/07	01/06/07	Decay	
4U 1543−47	U1543−D02	14/07/02	31/07/02	Decay	9,10
XTE J1550−564	J1550−R98	08/09/98	16/10/98	Rise	1, 2, 3
	J1550−R00	10/04/00	05/06/00	Rise	1, 2, 3
	J1550−D00	05/06/00	16/07/00	Decay	1,2,3
XTE J1650−500	J1650−R01	06/09/01	28/09/01	Rise	7
	J1650−D01	19/11/01	25/11/01	Decay	7
H 1743−322	H1743−R03	28/03/03	27/04/03	Rise	3
	H1743−D03	15/10/03	03/11/03	Decay	
XTE J1859+226	J1859−R99	09/10/99	27/10/99	Rise	6
Cyg X-1	CYGX1	15/06/01	01/12/02	Mixed	

References. (1) Rodriguez et al. 2003; (2) Rodriguez et al. 2004; (3) McClintock et al. 2007; (4) Belloni et al. 2006; (5) Belloni et al. 2005; (6) Casella et al. 2004; (7) Rossi et al. 2004; (8) Trudolyubov et al. 2001; (9) Kalemci et al. 2005; (10) Park et al. 2004; (11) ST07; (12) Trudolyubov 2001; (13) Vignarca et al. 2003.

proposed for use as a tool to determine a BH mass (Titarchuk & Fiorito 2004, hereafter TF04). Shaposhnikov & Titarchuk (2007), hereafter ST07, employed this idea to measure the mass of a prominent BH source Cygnus X-1 (Cyg X-1) and obtained a BH mass of $M_{\mathrm{Cyg}X1} = (8.7 \pm 0.8)\ M_{\odot}$, which has a better precision than conventional dynamical methods. Scaling arguments were also used to estimate masses in a number of ultraluminous X-ray sources (Fiorito & Titarchuk 2004; Dewangan et al. 2006; Strohmayer et al. 2007). In this paper, we further explore this technique by analyzing more representative data sets from Galactic BH sources. We concentrate our efforts on the study of correlations between the spectral index and characteristic subsecond variability frequencies and the total accretion disk luminosity. These two correlation patterns carry the most direct information on the BH mass and source distance. We also investigate the possibility that the shape of the correlation pattern can provide a direct signature of the bulk motion (converging) flow onto a BH or, in other words, the signature of a BH (see Titarchuk & Zannias 1998; Laurent & Titarchuk 1999, for more details on this subject). We present observational and theoretical arguments that the index–mass accretion rate saturation effect is a signature of a converging flow, when the mass accretion rate exceeds the Eddington limit, which can only exist in BH sources.

In the study presented, we enhance the scaling method by considering joint scaling of the spectral index in both the QPO frequency and disk component normalization (disk flux) domains. In the LHS and IS, only a small part of the disk emission component is seen directly. The energy spectrum is dominated by a Comptonized component seen as a power law. To calculate the total normalization of the "seed" disk blackbody (BB) component, we model the spectrum with a generic Comptonization model, which consistently convolves a disk BB with Green's (response) function of the Compton corona (CC) to produce the Comptonized component (see details in Section 2). Calculated in this way, the spectrum normalization is directly related to the BH mass, emission efficiency, source distance, and geometry. This allows us to apply the total disk normalization as an additional scaling variable and to impose an additional constraint on the BH mass and distance ratios. Thus, we use the index–QPO and index–disk normalization correlations to constrain the BH masses and distances for Galactic BH sources H 1743−322, GX 339−4, XTE J1550−564, XTE J1650−500, 4U 1543−47, XTE J1859+226, and Cyg X-1 based on their expected dependences on the mass of the central BH, the source distance, and the geometry. As our reference values for the scaling measurements, we use the previously measured BH mass, system distance, and inclination for Galactic microquasar GRO J1655−40.

The description of *Rossi X-Ray Timing Explorer* (*RXTE*) data for each source is given in Section 2. We provide the details of state transitions analysis in Section 3 and we present the results of the scaling method applied to the data in Section 4. We present a physical picture of the accretion process, which is consistent with the observed phenomenology of state transitions, in Section 5. Specifically, it provides a theoretical basis and an explanation for the observed scaling index–QPO and index–normalization patterns. We present theoretical arguments for the inverse proportionality of the QPO frequency on the BH mass in Section 5.1. We discuss the signature of bulk motion Comptonization (BMC) and its relation with the index evolution during the state transition in Section 5.2. Specifically, we show that the index saturation effect is a direct consequence of the existence of the innermost bulk motion region and, therefore, can be considered as an observational signature of a BH. In Section 6, we summarize our results and compare BH masses and distances with those obtained by other methods. We also briefly discuss the alternative methods for BH mass determination from X-ray data. Conclusions follow in Section 7. In Appendix A, we provide the mathematical details of the transition layer (TL) model (Titarchuk et al. 1998, hereafter TLM98), which is the basis for the proposed scenario.

2. OBSERVATIONS AND DATA REDUCTION

For the study presented in this paper, we have analyzed data for 17 spectral transitions in seven BH transient sources observed with the *RXTE*. We also analyzed a subset of Cyg X-1 data taken during 2001–2002 when the source showed a transition from the LHS to the HSS. In Table 1, we summarize data for each transition and also provide references to previous analyses.

We use the archival *RXTE* data from the HEASARC.[8] We present *RXTE*/Proportional Counter Array (PCA) light curves and hardness ratios for all analyzed outbursts in the top panels of Figures 2–6. These diagrams are created using *RXTE* mission long data products provided by the *RXTE* team. Each data point is based on a separate pointed PCA observation. Each transition data set is indicated by a separate color. The black color indicates observations during the HSS or the extreme LHS, which are not used in our analysis.

RXTE/PCA spectra have been extracted and analyzed in the 3.0–50 keV energy range using the most recent release of PCA response calibration (ftool `pcarmf v11.1`). We calculated the rms-normalized Fourier PDSs from high time-resolution PCA mode data in the frequency range 0.01–1024 Hz. The relevant deadtime corrections to energy spectra and timing spectra have been applied following "The RXTE Cook Book" recipes and Revnivtsev et al. (2000) correspondingly. The PCA

[8] http://heasarc.gsfc.nasa.gov/

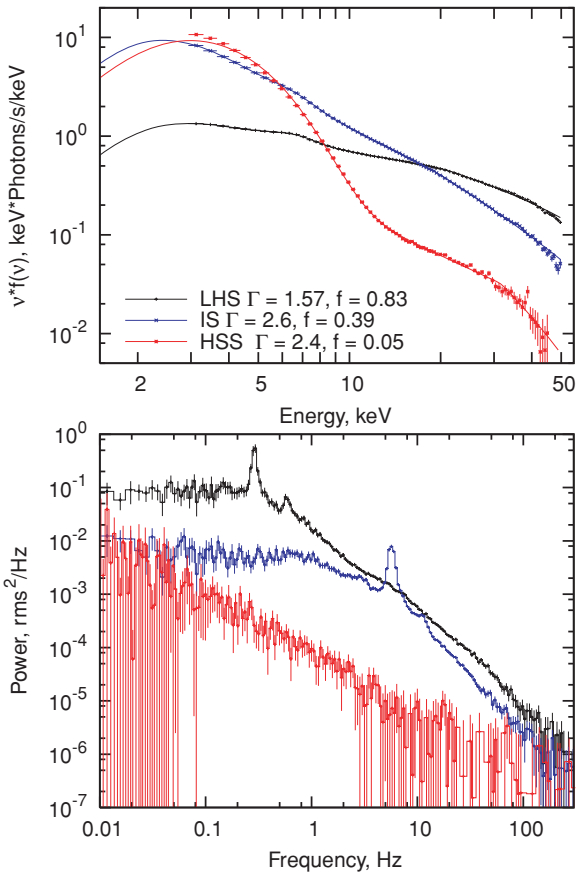

Figure 1. Three representative energy (top) and power (bottom) spectra during the rise part of the 1998 outburst of XTE J1550−564. Data are taken from *RXTE* observations 30188-06-01-00 (red), 30188-06-01-00 (blue), and 30191-01-05-00 (black). In the top panel, the solid curves correspond to the best-fit model spectra.

(A color version of this figure is available in the online journal.)

energy spectra were modeled using XSPEC astrophysical fitting software. Spectral analysis was done using an approach similar to that adopted in ST07 for Cyg X-1 and GRO J1655−40 data. To fit the PCA spectra, we used the sum of the *bmc* component (generic Comptonization model; see Titarchuk et al. 1997) and a Gaussian with the energy ∼ 6.5 keV, which is presumably due to an iron emission line. This model was also modified by the interstellar absorption, using the *wabs* model in XSPEC, with a hydrogen column value fixed at the Galactic value given by the nH HEASARC tool (Dickey & Lockman 1990) for a particular source and a high-energy cutoff (*highecut*). The width of the Gaussian was constrained in the range 0.8–1.2 keV. The high-energy cutoff component accounts for exponential overturn of the spectrum due to electron recoil effect. A systematic error of 1.0% have been applied to the analyzed spectra.

The *bmc* model describes the outgoing spectrum as a convolution of an input "seed" BB spectrum having normalization N_{bmc} and color temperature kT with a Green function for the Comptonization process. Similar to the ordinary *bbody* XSPEC model, the normalization N_{bmc} is a ratio of the source luminosity to the square of the distance:

$$N_{bmc} = \left(\frac{L}{10^{39}\ \mathrm{erg\ s^{-1}}}\right)\left(\frac{10\ \mathrm{kpc}}{d}\right)^2. \quad (1)$$

The resulting model spectrum is also characterized by a parameter $\log(A)$ related to a Comptonized fraction f, where $f = A/(1 + A)$ and Green's function spectral index $\alpha = \Gamma - 1$, where Γ is the photon index.

There are two reasons for using the *bmc* model. First, *bmc* by the nature of the model is applicable to the general case when photons gain energy not only due to thermal Comptonization but also via dynamic or BMC (see Titarchuk et al. 1997; Laurent & Titarchuk 1999; Shaposhnikov & Titarchuk 2006, for details). The second reason is that *bmc* calculates consistently the normalization of the "seed" photons N_{bmc}, presumably originating in the disk. The relation of N_{bmc} and its proportionality to the mass accretion rate in the disk is a direct consequence of the accretion disk theory (see, e.g., Shakura & Sunyaev 1973). The adopted spectral model well describes most data sets used in our analysis. The value of reduced χ^2-statistic $\chi^2_{\rm red} = \chi^2/N_{\rm dof}$, where $N_{\rm dof}$ is the number of degrees of freedom (dof) for a fit, is less than or around 1.0 for most of the observations. For a small fraction (less than 3%) of spectra with high counting statistic, the value of $\chi^2_{\rm red}$ reaches 1.5. However, it never exceeds a rejection limit of 2.0.

The PDS continuum shape in the LHS and IS has usually a band-limited noise shape, which is well presented by an empirical model $P_X \sim (1.0 + (x/x_*)^2)^{-in}$. The parameter x_* is related to the break frequency and $2 \times in$ is the slope of the PDS continuum after the break. We use the Lorentzian shape to fit QPO features. We quote the Lorentzian centroid as a QPO frequency.

Our approach to the analysis of a BH state transition is as follows. We identify a complete spectral transition as a period when the source state changes from the LHS to the HSS (or vice versa) showing gradual transition through the IS. In this paper, we analyze the transitions for which the frequency of *RXTE*/PCA pointing observations allows us to infer the index–QPO correlation patterns and to perform a comparative study. In Table 1, we provide a list of the transitions (outbursts) that we utilized in our study. In this table, we also introduce an ID name of each transition that consists of an abbreviated source name, dash, a transition direction identifier ("R" for the rise and "D" for the decay), and the two last digits of the year during which the event occurred. In Table 2, we present the details of the model fits to the spectral and timing data for each *RXTE* observation in the spectral transition.

3. CORRELATIONS BETWEEN SPECTRAL AND TIMING PROPERTIES DURING STATE TRANSITIONS

3.1. Phenomenology of the Correlation Behavior

Observations of Galactic BH X-ray binaries reveal diverse and dynamic phenomenology. The evolution of a BH binary in outburst usually is described in terms of its spectral states. The general picture of low/hard (LHS)–high/soft state (HSS) transition is illustrated in Figure 1 where we present energy and timing spectra of three representative *RXTE*/PCA observations of XTE 1550-564 for LHS, IS and HSS during 1998 outburst. It is important to note that upon entering into HSS the flat-top variability ceases, QPOs disappear and PDS acquires a pure power-law shape. The total variability in HSS is usually about 5% fractional rms. In Figures 2–6 (top panels), we show the spectral evolution of a given source throughout each analyzed outburst by presenting the PCA light curve and PCA hardness ratio. In the bottom panels from left to right, we plot the correlations of the photon index Γ versus the QPO frequency, *bmc* model normalization N_{bmc}, and Comptonized fraction $f = A/(A + 1)$. Data for a particular transition are

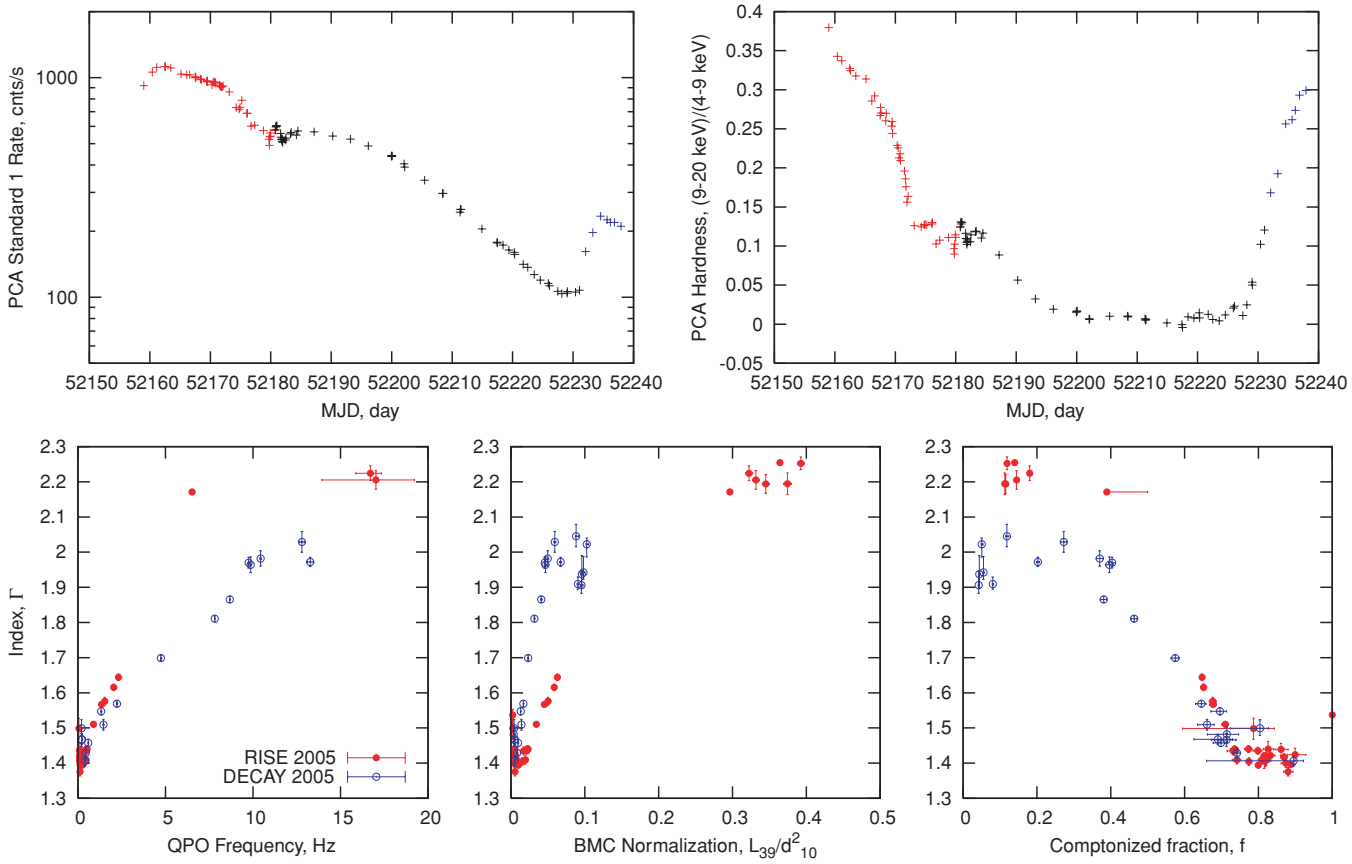

Figure 2. Top: PCA Standard 1 count rate (left) and hardness (right) for the 2005 outbursts from GRO J1655−40. Blue and red colors stand for rise and decay transitions, respectively. Bottom: photon index is plotted versus QPO frequency (left), BMC normalization (middle), and Comptonized fraction (right) for the rise (red) and the decay (blue) transitions.

(A color version of this figure is available in the online journal.)

distinguished using the same color legend for the correlation plots and the light-curve diagrams.

The general behavior of the correlations is as follows. The QPO frequency and normalization are positively correlated with the index. The Comptonization fraction and index are usually anticorrelated (see the right bottom panels in Figures 2–6). In the upper part of the correlation patterns, we observe a saturation of index that is more apparent in the index–normalization domain than in the index–QPO pattern. The reason for this is that the index and normalization values, as the best-fit parameters of the energy spectrum, are always available independent of the source state, while QPOs tend to faint as a source enters the HSS.

In ST07, we claimed the presence of index saturation in Cyg X-1, GRO J1655−40 and GRS 1915+105 using correlations with the QPO frequency. Here we confirm the index saturation effect for GRO J1655−40 and Cyg X-1 (see Figures 2 and 6). Moreover, we establish the index saturation effect in GX 339−4, H 1743−322, 4U 1543−47, and XTE J1650−500 (see Figures 3–5 and 8 respectively). It is important to mention that the saturation of index with respect to the photon spectrum normalization (mass accretion rate) in XTE J1650−500 was also recently established by Montanari et al. (2008) in their analysis of *BeppoSAX* data from 2001 outburst.

Three rise transitions, J1550−R98, H1743−R03, and J1859−R99, exhibit similar behavior. For all these transitions, when the index reaches its high values (greater than 2.5), the Comptonization fraction shows nonmonotonic behavior. Namely, for J1550−R98 and H1743−R03, as the source leaves the LHS, f starts to decrease as expected. However, when the source enters the IS, the index-f track reverses and f returns back to its maximum value of 1.0. In Figure 4, we illustrate this evolution of the Comptonization fraction f as a function of photon index Γ for the rise transition H1743−R03 (see the red data points on the right bottom panel).

During the decay transitions the source luminosity is lower than that for the rise episodes and the corresponding variability is suppressed, which is probably due to lower excitation power in the accretion flow (see Titarchuk & Shaposhnikov 2008, for details). As a result, the spectral and timing data related to the decay transitions have a lower signal-to-noise ratio (S/N) than those for the rise transitions. The index saturation levels for the decay stages have values close to 2.1. Most probably, this is due to the fact that at low accretion rates during an outburst decay the cooling of the X-ray emission area (Comptonization cloud) by the disk photons is less efficient than that at high $\dot{M}$. As a result, the CC plasma temperature T_e is higher, leading to more efficient Comptonization and a harder spectrum. This direct connection between the temperature of the CC and the hardness of the emergent spectrum was shown by Monte Carlo simulations in Laurent & Titarchuk (1999). In other words, the decay transitions appear to be different from the rise transitions: correlation patterns are not scalable in the normalization domain and they are usually not self-similar given

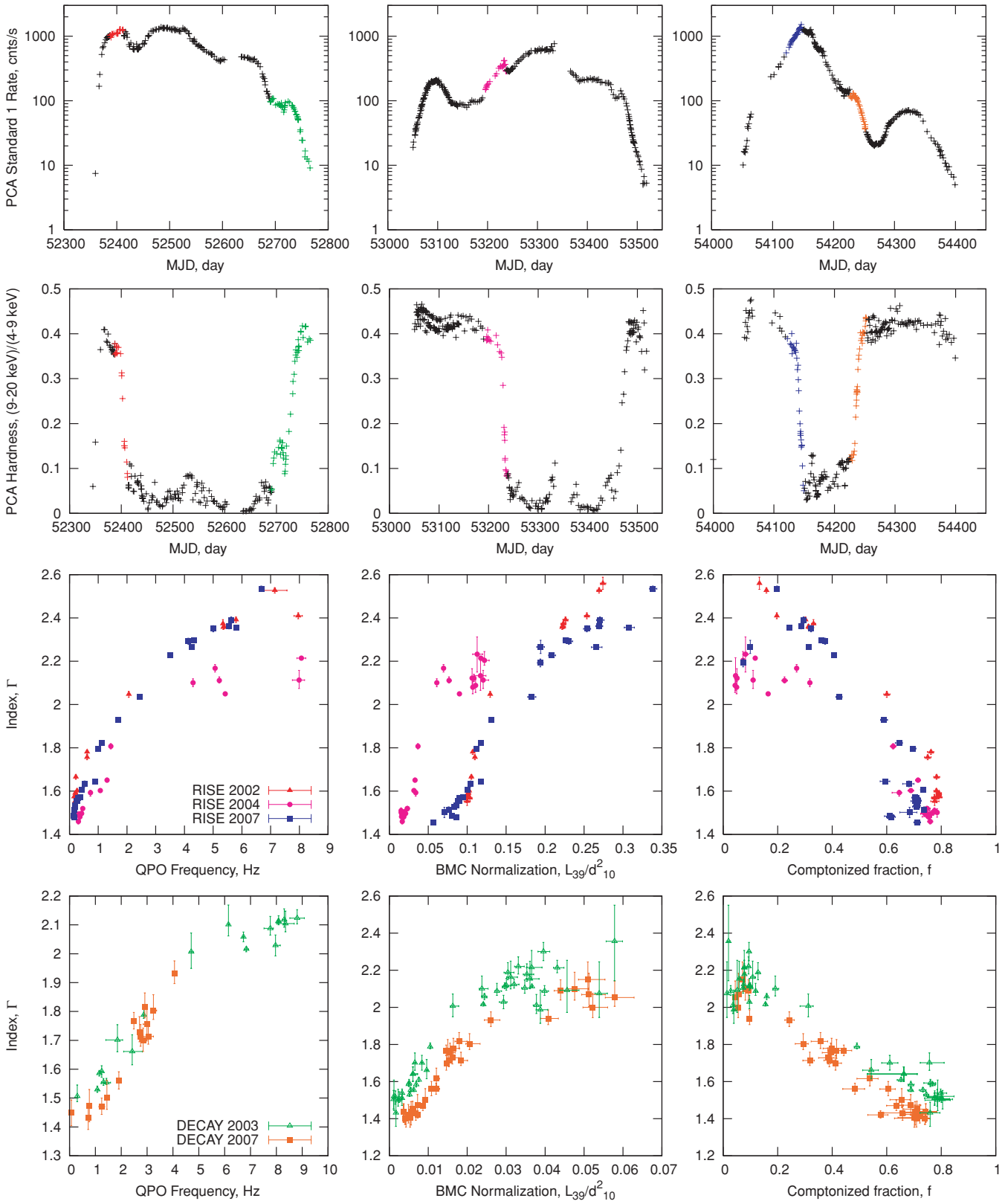

Figure 3. PCA Standard1 count rate (top row) and hardness (second row) for three outbursts from GX 339−4 on 2002 (left), 2004 (middle), and 2007 (right). Third and bottom rows: photon index plotted versus QPO frequency (left), BMC normalization (middle), and Comptonized fraction (right) for transitions in GX 339−4 (each transition is indicated by a different color).

(A color version of this figure is available in the online journal.)

that the index saturations take place at different levels. Our experience shows that while decay-to-decay and rise-to-rise scalings produce consistent results, the decay-to-rise pattern scaling is not a reliable mass–distance indicator.

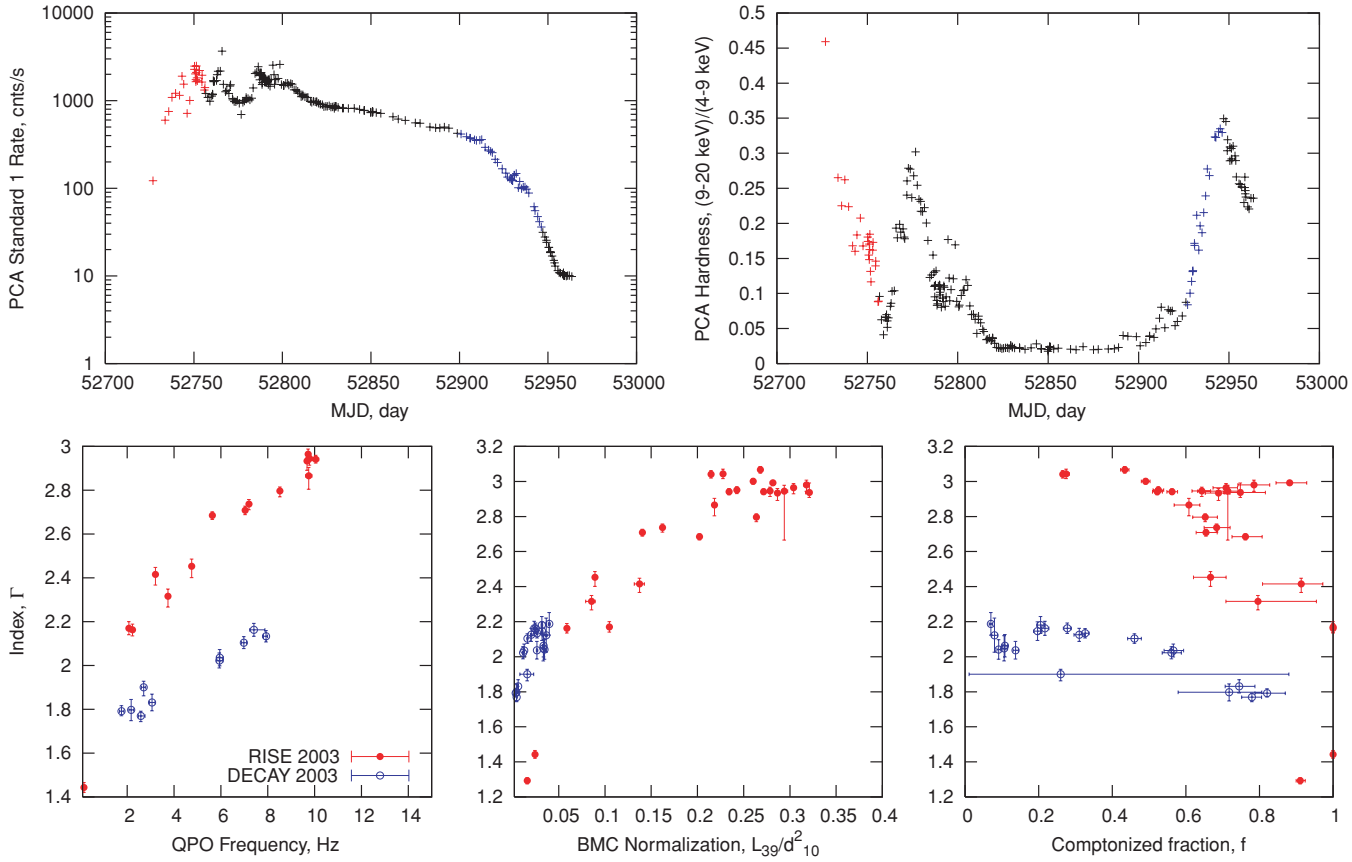

Figure 4. Top: PCA Standard 1 count rate (left) and hardness (right) for the 2003 outbursts from H1743−322. Bottom: photon index plotted versus QPO frequency (left), BMC normalization (middle), and Comptonized fraction (right) for the rise and the decay transitions.
(A color version of this figure is available in the online journal.)

To illustrate the above points, let us consider the properties of state transitions in GX 339−4. In this source, five different (rise and decay) transitions exhibited five different tracks (see the third and fourth row panels from the top in Figure 3). Two rise transitions, GX339−R02 and GX339−R07, occurred at higher fluxes than that for two decay transitions, GX339−D03 and GX339−D07. These rise transitions also showed steeper index–QPO (index–normalization) correlations with higher saturation levels. The difference between these transitions is clearly seen. On the other hand, the GX339−R04 hard-to-soft transition resembles a decay track with the index saturated at a value of 2.15 and a lower luminosity. But even for this rise episode, the index–normalization track is much steeper than those for the decay episodes. The decay transition during the 2004 outburst was quick and did not show sufficient QPO activity. We, therefore, discarded this transition episode from our analysis.

It is also worthwhile to discuss the behavior of XTE J1550−564 during the 1998 rise outburst in detail. The outburst started on MJD 51063 and went through the initial LHS phase, which ended on MJD 51069. During this period, the spectral index increased from 1.35 to 2.2 and the QPO frequency changed from 0.3 to 3.3 Hz. In Figure 7, this stage is marked by filled black circles. For the following 10 days, the source exhibited an IS with a strong flare on MJD 51076, when the index and QPO frequency peaked at 2.8 and 14 Hz correspondingly (IS–VHS track). We mark these data points by filled red circles. After the flare, the source returned to the IS with index $\sim$ 2.3 and QPO at $\sim$3 Hz. For the next 20 days, we observed smooth evolution toward the HSS with the index slightly increasing to 2.5 and the QPO frequency rising to $\sim$ 5 Hz. On about MJD 51105, the source entered the HSS (IS–HSS track). The index–QPO correlation consists of two different tracks, which are shown in Figure 7. The correlation curve related to the IS–HSS stage lies lower than that related to the IS–VHS transition. Clearly, the conditions in the accretion flow changed between these episodes. During the IS–VHS stage, the source presumably went through the strongest surge of accretion. This cold accretion flow provided strong cooling, which is manifested by a higher spectral index. These changes in the physical conditions in the accretion flow led to a double-track pattern of the correlation. Therefore, for the scaling purposes we treat a combination of the initial LHS with IS–VHS and IS–HSS data as two separate correlation patterns. We further refer to them as J1550−98Ra and J1550−98b, respectively.

We revisited the data for GRO J1655−40 and Cyg X-1, which were used for BH mass measurement in Cyg X-1 (ST07). We present the data for these sources in Figures 2 and 6. In fact, Cyg X-1 is a persistent source, with somewhat different phenomenology from the other sources analyzed in this study. The Cyg X-1 data obtained during 2001 and 2002 were chosen for the analysis (see Figure 6). In the 2001–2002 period the source exhibited two transitions, from the LHS to the HSS (red data points) and a reverse transition marked by the blue color. The black points indicate the observation when the source was in the HSS. As seen from the lower panels, the rise and the decay data from Cyg X-1 are very similar in terms of the index–QPO and index–normalization correlations. In particular, the same

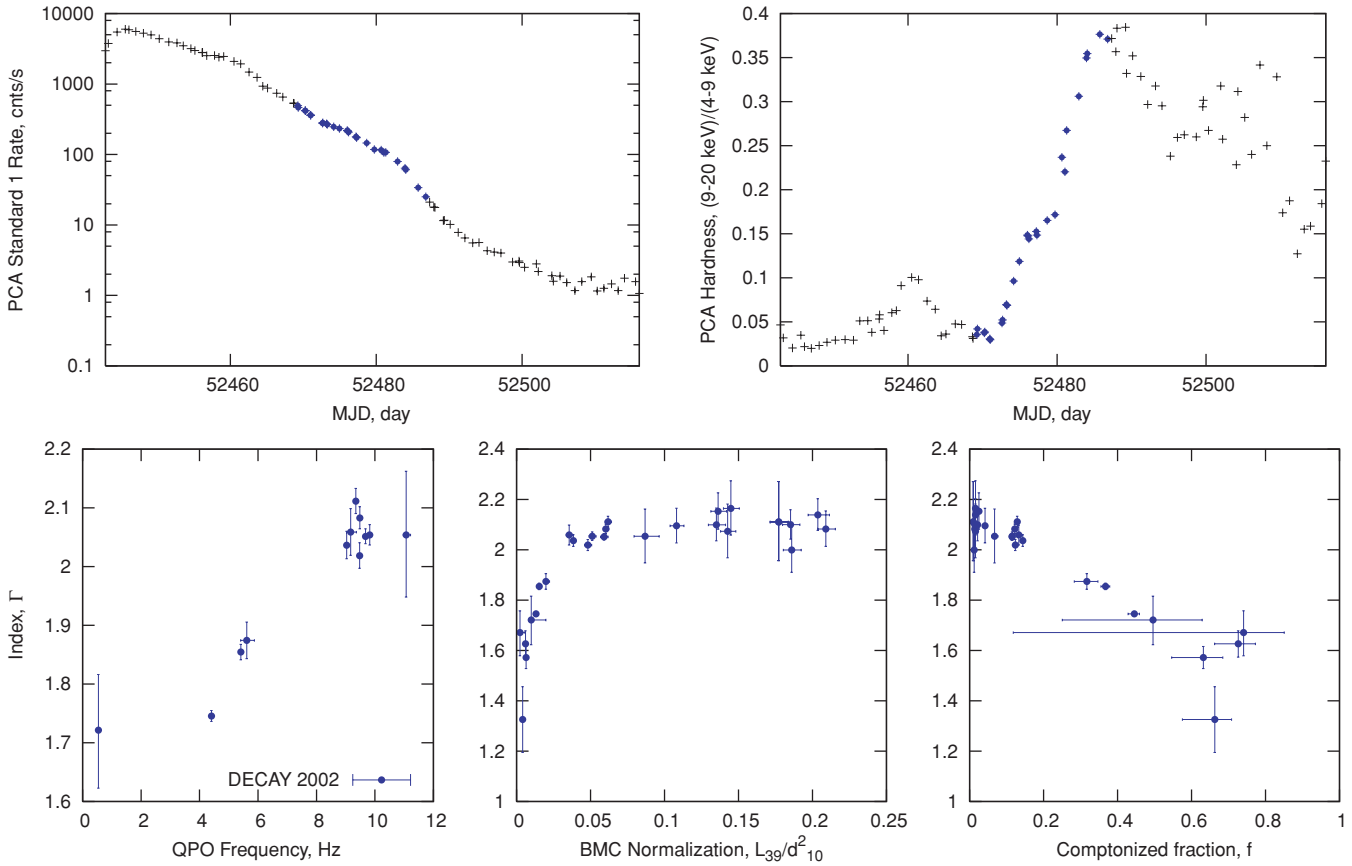

Figure 5. Top: PCA Standard 1 count rate (left) and hardness (right) for the 2002 outburst from 4U 1543−47. Bottom: photon index versus QPO (left), BMC normalization (middle), and Comptonized fraction (right) for the decay transition.

(A color version of this figure is available in the online journal.)

index–normalization tracks indicate that there is no hysteresis effect in this source. This may be related to the persistent nature of the accretion or the O-star wind. We, thus, use both the rise and the decay data for Cyg X-1 data as one data set to construct the correlation pattern. This approach is consistent with that adopted in the ST07 analysis.

3.2. The Scaling Technique and Parameterization of the Correlation Patterns

One of the goals of the presented study is to apply X-ray observational data from BH sources to infer their fundamental characteristics. To do this, we use the BH state paradigm combined with the scaling laws expected to be observed in spectral and timing data during state transitions.

First, using available X-ray observations we verify a theoretical conjecture that the QPO low frequency is inversely proportional to a BH mass $m = M_{\rm bh}/M_\odot$ (see TLM98; TF04). This QPO frequency dependence on m is a simple consequence of the fact that all characteristic dynamical timescales in an accreting flow onto a compact object are set by the mass of the object (see, e.g., Shakura & Sunyaev 1973, and Section 5.1). Thus, QPO frequencies, being in an inverse proportion to these timescales, have to be inversely proportional to m. This intuitive law of nature now finds its observational confirmation. In Section 5.1, we present theoretical arguments for the inverse dependence of the QPO frequencies on m in terms of the TL model (see details in TLM98; TF04; Appendix A).

Thus, we write the first scaling law (that we implement in our scaling technique for the BH mass determination) in terms of a scaling factor:

$$s_\nu = \frac{\nu_r}{\nu_t} = \frac{M_t}{M_r}, \tag{2}$$

where subscripts r and t of frequency ν denote the reference and target sources, respectively.

The second scaling law, which we use as a basis for our mass and distance determination analysis, relates a source flux F detected by an observer on the Earth, a disk flux L, and distance d, namely

$$\frac{F_r}{F_t} = \frac{L_r}{L_t}\frac{d_t^2}{d_r^2}. \tag{3}$$

The disk flux L can be represented as

$$L = \frac{GM_{\rm bh}\dot{M}}{R_*} = \eta(r_*)\dot{m}L_{\rm Ed}. \tag{4}$$

Here $R_* = r_* R_S$ is an effective radius where the main energy release takes place in the disk, $R_S = 2GM/c^2$ is the Schwarzschild radius, $\eta = 1/(2r_*)$, $\dot{m} = \dot{M}/\dot{M}_{\rm crit}$ is the dimensionless mass accretion rate in units of the critical mass accretion rate $\dot{M}_{\rm crit} = L_{\rm Ed}/c^2$, and $L_{\rm Ed}$ is the Eddington luminosity.

On the other hand,

$$L_{\rm Ed} = \frac{4\pi GMm_p c}{\sigma_T}, \tag{5}$$

that is, $L_{\rm Ed} \propto M$ and thus using Equations (4) and (5) we have that

$$L \propto \eta(r_*)\dot{m}m. \tag{6}$$

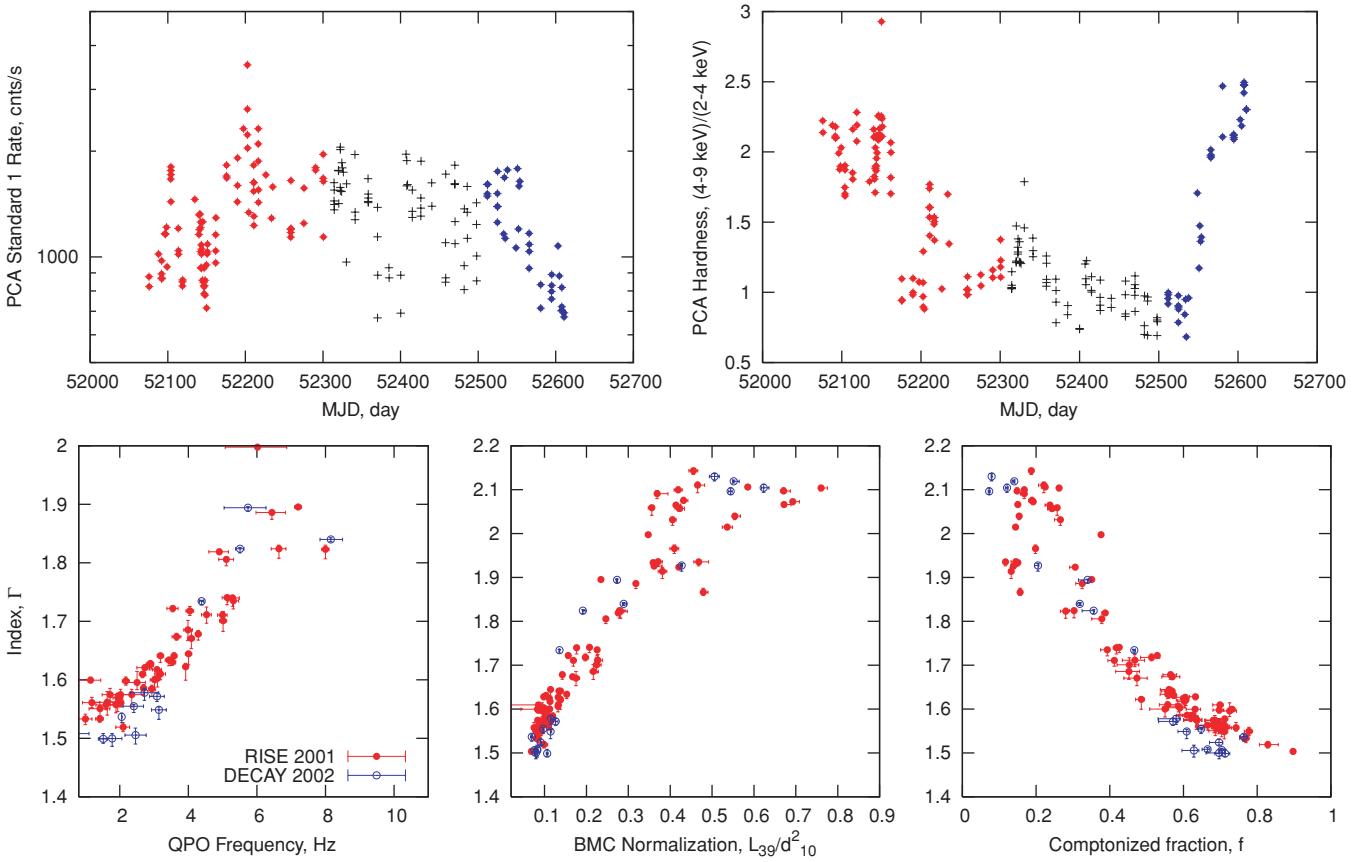

Figure 6. Top: PCA Standard 1 light curve (left) and hardness (right) for Cyg X-1 during 2001–2002. Red points indicate soft-to-hard transition while blue points show hard-to-soft transition. Observations during the HS are shown in black color. Bottom: photon index vs. QPO (left), BMC normalization (middle), and Comptonized fraction (right) during 2001–2002 state transitions in Cyg X-1.

(A color version of this figure is available in the online journal.)

Note that both $\dot{m}$ and η are assumed to be the same for two different sources in the same spectral state, which leads to $L_r/L_t = M_r/M_t = 1/s_\nu$. In our spectral analysis we determine the normalization of "seed" radiation, which is supplied by an accretion flow (disk) prior to Comptonization. The ratio of these normalizations for target and reference sources in the same spectral state can be written as

$$s_N = \frac{N_r}{N_t} = \frac{L_r}{L_t}\frac{d_t^2}{d_r^2} f_G. \tag{7}$$

Here, f_G is a geometrical factor which takes into account the difference in the viewing angles of the seed photon emission area (the inner disk) by the Earth observer for two given analyzed sources. Therefore, in the case of radiation coming directly from the disk it would have the value $f_G = (\cos\theta)_r/(\cos\theta)_t$, where θ is the inclination angle of the inner disk. Note that this form of f_G, however, may not be very accurate because the geometry of both the inner disk and the corona can be different from the plane (disk) geometry. In fact, in BH states of interest (LHS and IS) they can be described, for instance, by quasi-spherical configuration. Despite this uncertainty in the determination of f_G, we adopt the above form f_G in which $\theta \sim i$ if information on the system inclination angle i is available. In doing this, we introduce an additional assumption that the inner accretion disk and the system inclination angles are the same. This assumption, however, proved to be in good agreement with our analysis.

Now we write the final equations of our scaling analysis. Namely, when s_ν and s_N are measured, the mass and the distance of the target source can be calculated as

$$M_t = s_\nu M_r \tag{8}$$

and

$$d_t = d_r \left(\frac{s_\nu s_N}{f_G}\right)^{1/2}. \tag{9}$$

The part of the scaling method presented by Equation (9) is new. In the previous analysis (see ST07), we only use the scaling factor of the index–QPO correlation s_ν and apply it for the determination of the BH mass distribution.

The new modified technique uses timing information and the normalization of the photon spectrum to constrain both the BH mass and the distance for a target source, provided that these quantities are known for a reference source.

With Equations (8) and (9) in hand, the task of BH mass and distance measurements for a target source is reduced to the determination of scaling coefficients s_ν and s_N with respect to the data for a reference source. The appropriate technique has already been implemented in ST07. Specifically, after scalable state transition episodes are identified for two sources, the correlation pattern for a reference transition is parameterized in terms of the analytical function

$$f(x) = A - D\,B \ln\left[\exp\left(\frac{1.0 - (x/x_{\rm tr})^\beta}{D}\right) + 1\right], \tag{10}$$

where argument x is either the QPO frequency ν or normalization N_{bmc}. By fitting this functional form to the correlation

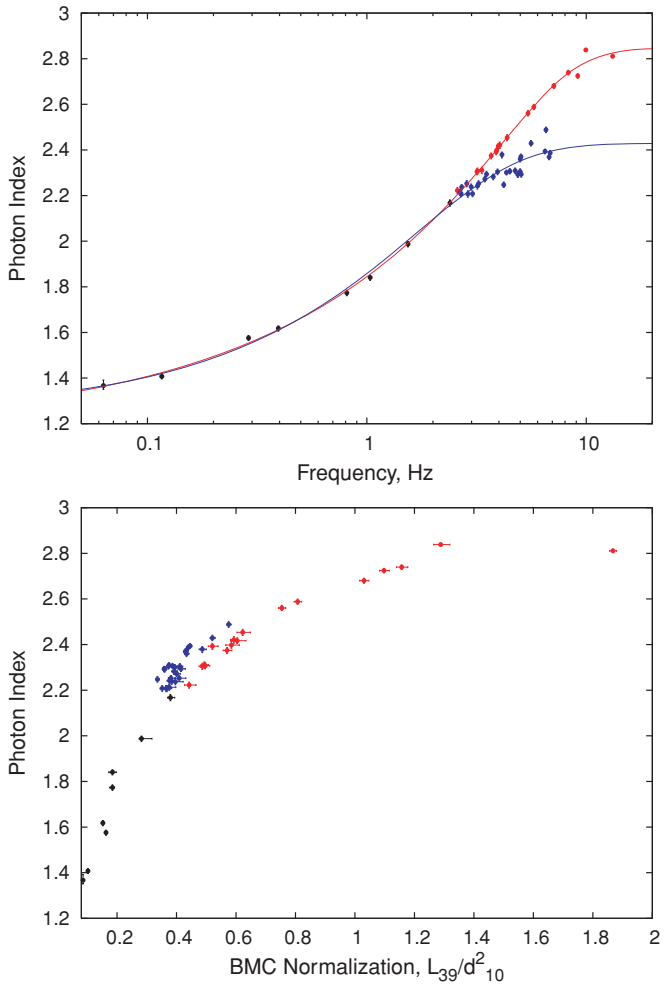

Figure 7. Photon index–QPO frequency and index-BMC normalization correlations (upper and bottom panels, respectively) during the rise of XTE J1550−564 1998 outburst. Index–QPO correlation exhibits two different tracks, which correspond to different index saturation levels (see text for details).

(A color version of this figure is available in the online journal.)

pattern, we find a set of parameters A, B, D, $x_{\rm tr}$, and β that represent a best-fit form of the function f for a particular correlation curve.

For $x \gg x_{\rm tr}$, the correlation function $f(x)$ converges to a constant value A. Thus, A is a value of the index saturation level, β is the power-law index of the part of the curve for lower argument values and $x_{\rm tr}$ is the frequency/normalization at which the index levels off. Parameter D controls how fast the transition occurs. We scale it to a target pattern by a transform $x \rightarrow sx$ when the best fit is found for a reference pattern.

The use of the analytical function to parameterize the correlations allows us to avoid the theoretical modeling of the index–QPO relation based on any particular physical model, which would require some internal parameterization in any case (see discussion in ST07). It makes the scaling procedure model independent, and it is justified because it satisfactorily represents both the index–QPO and the index–normalization patterns.

4. BH MASS AND DISTANCE MEASUREMENT IN XRBS

The Galactic microquasar GRO J1655−40 is a well-studied BH XRB with the best measured mass and distance among known stellar mass BH sources. We therefore use this system as a primary reference source for our scaling. In addition, ancillary information on the system inclination is available, which makes distance determination more reliable. However, not all sources we analyze here have transitions directly scalable to GRO J1655−40 data. Therefore, we have to utilize an intermediate reference source to provide measurements for all sources. Specifically, only GX 339−4 and 4U 1543−47 have transitions that are scalable to our primary reference source. After measuring the BH mass and distance for GX 339−4, we use this source as a reference for XTE J1550−564 and XTE J1650−500. Note that this scaling between GX 339−4 and XTE J1650−500 was allowed with both rise and decay data. We then use XTE J1550−564 as a reference source for scaling to H 1743−322 and XTE J1859−226 data. Finally, we measure the BH mass and distance for Cyg X-1 by scaling to GRO J1655−40 and 4U 1543−47, respectively. All measurements are summarized in Table 3 and illustrated in Figures 8 and 9. Below, we provide some details on how we combine our scalings in chains to provide measurements for all sources of interest.

We first determine parameters for sources that have correlation patterns self-similar to GRO J1655 data. Namely, data sets GX399−D07 and U1543−D02 are scalable to that of J1655−D05. These scalings provide BH mass measurements for GX 339−4 and 4U 1543−47 (Figure 8, panels (A) and (B)). Other decay transitions (i.e., GX339−D03, J1650−D01, and J1743−D03) have slightly higher saturation levels of ∼2.1 and present a different cluster of scalable patterns (data sets). Thus we use GX339−4 as a reference source to provide the mass-distance determinations for XTE J1650−500 (Figure 8, panel (D)) and H 1743−322 (Figure 8, panel (F)). We use GX339−R04 data to scale to XTE J1550−564 (J1550−R00) data and to measure the BH mass and distance in XTE J1550−564 (Figure 8, panel (C)). The resulting value of the BH mass is in an excellent agreement with the dynamical determination of the BH mass in XTE J1550−564. We also scale the rise transition data sets GX339−R04 and J1650−R01 (Figure 8, panel (E)) to provide a double check with the decay data scaling (see Figure 8, panel (D)) for the same sources. The results obtained with these parallel scalings are in a striking agreement.

Finally, we use XTE J1550−564 (J1550−R98) data for scaling with H 1743−322 (1743−R03) and XTE J1859−226 (J1859−R99) (Figure 9, panels (G) and (H) correspondingly). As we mentioned in the previous section, during the 1998 outburst rise from XTE J1550−564, the index exhibited two correlation tracks with different saturation levels. The initial LHS combined with the subsequent IS–VHS phase is similar to the H 1743−322 transition observed during the 2003 rise episode (1743−R03). We therefore use this subset of XTE J1550 (J1550−R98a) to scale to the 1743−R03 data. The IS–HSS phase of J1550−R98 data is scalable with the J1859−R99 transition (Figure 9, panel (H)). We also note that these outbursts (J1550−R98, J1859−R99, and H1743−R03) are similar not only in terms of the index–QPO and index–normalization behavior but also in terms of the index-f patterns and the overall appearance of outburst light curves (we illustrate these observational appearances in Figure 4, which presents data for H 1743−322).

Finally, in Figure 9 (panel (K)), we show the scaling between J1655−D05 and CYGX1 data sets (see Table 1 for these data set descriptions). In Table 3, we present the scaling coefficients S_ν and S_N obtained using our scalings procedure. We also provide BH masses and distances obtained using the calculated scaling

Table 2
Spectral and Timing Characteristics for *RXTE* Data[a]

Transition ID	Observation ID	MJD[b] (day)	BH State	ν_{QPO} (Hz)	α	kT (keV)	log(A)	N_{bmc} $L_{39}/d^2{}_{10}$	$E_{\rm cut}$ (keV)	$E_{\rm fold}$ (keV)	$F_X \times 10^8$ (erg s^{-1} cm^{-2})	$\chi^2{}_{\rm red}$
GX339−R07	92428-01-02-00	54122.27	LHS	...	0.455(9)	0.61(3)	0.39(3)	0.0566(8)	26(3)	76(14)	0.872(2)	0.82
	92428-01-03-00	54127.11	LHS	...	0.50(2)	0.55(5)	0.33(6)	0.070(2)	28(6)	50(29)	1.089(9)	0.93
	92035-01-01-00	54129.47	LHS	0.164(6)	0.51(1)	0.65(3)	0.44(2)	0.076(1)	21(2)	95(9)	1.160(2)	0.73
	92035-01-01-01	54128.94	LHS	0.142(3)	0.484(8)	0.53(2)	0.19(3)	0.080(1)	26(1)	66(6)	1.137(3)	0.87
	92035-01-01-02	54131.10	LHS	0.180(4)	0.527(9)	0.59(3)	0.38(3)	0.0834(9)	26(1)	67(6)	1.276(3)	1.03
	92035-01-01-03	54130.13	LHS	0.167(4)	0.48(1)	0.55(2)	0.20(3)	0.086(1)	22(1)	73(6)	1.214(3)	0.86
	92035-01-01-04	54132.08	LHS	0.200(3)	0.53(1)	0.59(3)	0.39(3)	0.085(1)	24(1)	71(6)	1.314(2)	1.03
	92035-01-02-00	54133.00	LHS	0.237(8)	0.55(1)	0.58(3)	0.39(3)	0.088(1)	25(4)	72(19)	1.354(3)	0.90
	92035-01-02-01	54133.92	LHS	0.264(6)	0.554(9)	0.59(3)	0.37(3)	0.0899(9)	25.2(9)	68(6)	1.362(3)	0.98
	92035-01-02-02	54135.03	LHS	0.296(4)	0.569(9)	0.57(3)	0.38(3)	0.090(1)	24.5(8)	60(4)	1.380(3)	0.83
	92035-01-02-03	54136.02	LHS	0.361(6)	0.56(1)	0.60(3)	0.37(3)	0.094(1)	22.7(9)	72(5)	1.414(3)	1.16
	92035-01-02-04	54137.00	LHS	0.432(5)	0.60(1)	0.62(3)	0.43(2)	0.100(1)	22.8(8)	70(4)	1.510(3)	0.76
	92035-01-02-08	54137.85	LHS	0.53(2)	0.63(1)	0.54(3)	0.33(4)	0.104(2)	21(1)	78(8)	1.522(3)	0.98
	92035-01-02-07	54138.83	LHS	0.900(5)	0.64(1)	0.52(2)	0.16(3)	0.117(2)	21.6(7)	68(3)	1.521(3)	0.78
	92035-01-02-06	54139.94	IS	0.987(5)	0.79(1)	0.61(2)	0.36(2)	0.111(1)	21.9(7)	65(3)	1.466(2)	0.73
	92035-01-03-00	54140.20	IS	1.136(2)	0.82(1)	0.56(2)	0.25(3)	0.117(2)	21.0(8)	75(5)	1.438(2)	0.72
	92035-01-03-01	54141.05	IS	1.691(3)	0.92(1)	0.55(2)	0.15(2)	0.131(2)	20.6(9)	79(6)	1.384(3)	0.74
	92035-01-03-02	54142.04	IS	2.434(9)	1.03(1)	0.51(1)	−0.14(2)	0.182(5)	20.6(8)	72(5)	1.343(2)	0.85
	92035-01-03-03	54143.02	IS	3.508(9)	1.22(1)	0.55(1)	−0.17(1)	0.208(4)	24(1)	67(10)	1.338(2)	0.91
	92428-01-04-00	54143.87	IS	4.34(1)	1.29(1)	0.597(9)	−0.25(1)	0.226(3)	22(1)	80(11)	1.337(3)	1.00
	92428-01-04-01	54143.95	IS	4.24(1)	1.26(1)	0.52(1)	−0.35(1)	0.265(7)	22(1)	87(14)	1.336(3)	1.08
	92428-01-04-02	54144.09	IS	4.13(2)	1.29(1)	0.57(1)	−0.23(1)	0.230(5)	22(3)	125(46)	1.361(3)	0.97
	92428-01-04-03	54144.87	IS	5.00(2)	1.35(1)	0.59(1)	−0.33(1)	0.253(5)	25(3)	81(33)	1.346(4)	1.31
	92428-01-04-04	54145.96	IS	5.63(2)	1.39(1)	0.597(9)	−0.38(1)	0.270(5)	22(2)	89(33)	1.346(3)	1.17
	92035-01-03-05	54145.11	IS	5.80(2)	1.35(1)	0.554(8)	−0.50(1)	0.307(6)	25(2)	81(17)	1.303(3)	1.37
	92035-01-03-06	54146.03	IS	5.55(2)	1.36(1)	0.601(8)	−0.40(1)	0.269(4)	21(2)	111(24)	1.343(2)	1.29
	92035-01-04-00	54147.01	IS	6.67(2)	1.53(1)	0.626(7)	−0.608(9)	0.338(5)	...	...	1.371(3)	1.59
	92035-01-04-01	54148.14	IS	...	1.26(3)	0.796(7)	−0.96(1)	0.194(5)	...	...	1.024(6)	1.07
	92035-01-04-02	54149.69	HSS	...	1.19(2)	0.782(4)	−1.104(8)	0.193(4)	...	...	0.963(6)	1.27

Notes.
[a] Table in the paper/PDF version includes only data for GX339−R07 transition.
[b] Date at the start of the *RXTE* observation.
(This table is available in its entirety in a machine-readable form in the online journal. A portion is shown here for guidance regarding its form and content.)

Table 3
Index–QPO and Index-Norm Scaling Coefficients

Target Tr. ID	Reference Tr. ID	Figure 8 Panel	S_ν	S_N	m	d	f_G
GX339−D07	J1655−D05	A	1.96 ± 0.12	1.65 ± 0.06	12.3 ± 1.4	5.75 ± 0.64	1
GX339−R04	J1655−R05		1.95 ± 0.19	1.9 ± 0.1	12.3 ± 1.8	6.15 ± 0.83	1
U1543−D03	J1655−D05	B	1.49 ± 0.15	2.23 ± 0.22	9.4 ± 1.4	3.5 ± 0.5	0.37
J1550−R00	GX339−R04	C	0.87 ± 0.02	0.37 ± 0.02	10.7 ± 1.5	3.3 ± 0.5	1
J1650−D01	GX339−D03	D	0.80 ± 0.02	0.47 ± 0.01	9.9 ± 1.4	3.5 ± 0.5	1
J1650−R01	GX339−R04	E	0.76 ± 0.02	0.358 ± 0.004	9.3 ± 1.2	2.95 ± 0.4	1
H1743−D03	GX339−D03	F	1.15 ± 0.07	2.16 ± 0.13	12.7 ± 2.6	9.1 ± 2.0	1
H1743−R03	J1550−R98a	G	1.19 ± 0.08	6.44 ± 0.52	14.2 ± 2.4	9.1 ± 1.6	1
J1859−R99	J1550−R98b	H	0.696 ± 0.015	0.429 ± 0.005	7.7 ± 1.2	4.2 ± 0.5	1
CYGX1	J1655−D05	K	1.17 ± 0.03	0.144 ± 0.003	7.4 ± 0.6	2.04 ± 0.18	0.42
CYGX-1	U1543−D03		0.85 ± 0.02	0.064 ± 0.001	8.0 ± 0.9	2.1 ± 0.4	0.42

Notes. [a] The column contains estimates for f_G based on available information on inclination angles.

Table 4
Parameterizations for Reference Patterns

Transition	B	Index–QPO		β	A	Index-Normalization			β
		$\nu_{\rm tr}$	D			B	$N_{\rm tr}$	D	
J1655−R05	0.59 ± 0.04	3.0 ± 0.1	1.0	1.6 ± 0.2	2.2	0.400 ± 0.003	0.061 ± 0.003	1.0	2.3 ± 0.6
J1655−D05	0.58 ± 0.01	10.9 ± 0.4	0.1	1.0	2.02 ± 0.02	0.44 ± 0.02	0.026 ± 0.002	1.0	1.88 ± 0.25
GX339−D03	0.66 ± 0.02	5.4 ± 0.4	0.1	1.0	2.08 ± 0.01	0.45 ± 0.02	0.010 ± 0.001	1.0	2.0 ± 0.3
GX339−R04	0.58 ± 0.02	1.4 ± 0.2	1.0	1.0	2.14 ± 0.01	0.51 ± 0.02	0.039 ± 0.002	1.0	3.5
J1550−R98a	1.27 ± 0.02	1.84 ± 0.07	1.0	0.65 ± 0.02	2.94 ± 0.08	1.8 ± 0.3	0.162 ± 0.05	1.0	0.6 ± 0.1
J1550−R98b	1.32 ± 0.03	1.97 ± 0.07	1.0	0.5	2.55	1.25 ± 0.04	0.164 ± 0.004	1.0	1.0

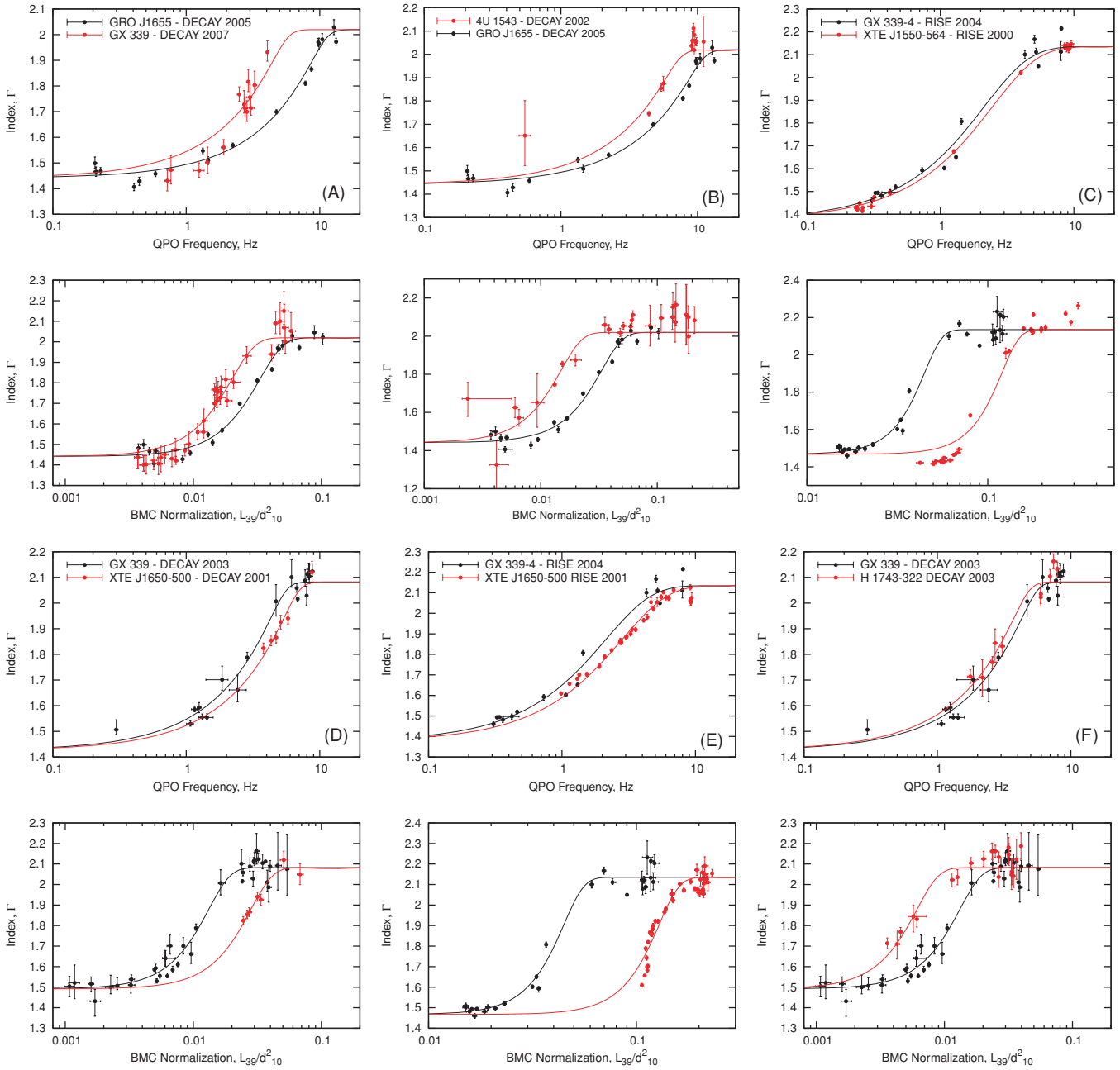

Figure 8. Scaling photon index vs. QPO frequency and normalization correlations for BH sources. The normalization plot is placed below the corresponding QPO frequency panel. In these diagrams, the target transition for scaling is shown in red color while reference transition is plotted in black. Each pair (from left to right and from top to bottom) corresponds to the row in Table 3 beginning with the second row.

(A color version of this figure is available in the online journal.)

coefficients and Equations (8) and (9). The parameterizations of reference patterns in terms of the empirical functional form $f(x)$ (Equation (10)) are presented in Table 4.

Thus, we construct the sequence of scalings that allows us to obtain the BH mass and the source distance for a number of BH XRBs (and in some cases to provide a double check for these measurements). Table 5 presents the final results of the BH mass and distance determinations using our scaling method along with independently reported masses, distances, and inclination angle values found in the literature. For the sources for which we were able to make parallel scaling measurements with two different data set pairs, the final best-fit values are the averages between individual measurements and the error ranges are calculated using the sum of error intervals given by individual scalings.

5. PHYSICAL SCENARIO FOR THE EVOLUTION OF SPECTRAL AND TIMING PROPERTIES DURING BH STATE TRANSITIONS

The accretion process onto a BH is far from being completely understood. Theoretical models that are available for astronomers to explain observational phenomena usually deal with only narrow aspects of a broad observational picture. For example, while there are several proposed QPO models in the literature (see Remillard & McClintock 2006, for references), most of them concern only the QPO phenomenology and lack the connection with spectral properties and state transition aspects. However, in the recent years, the concept of TL in the accretion flow has emerged. In the framework of this model,

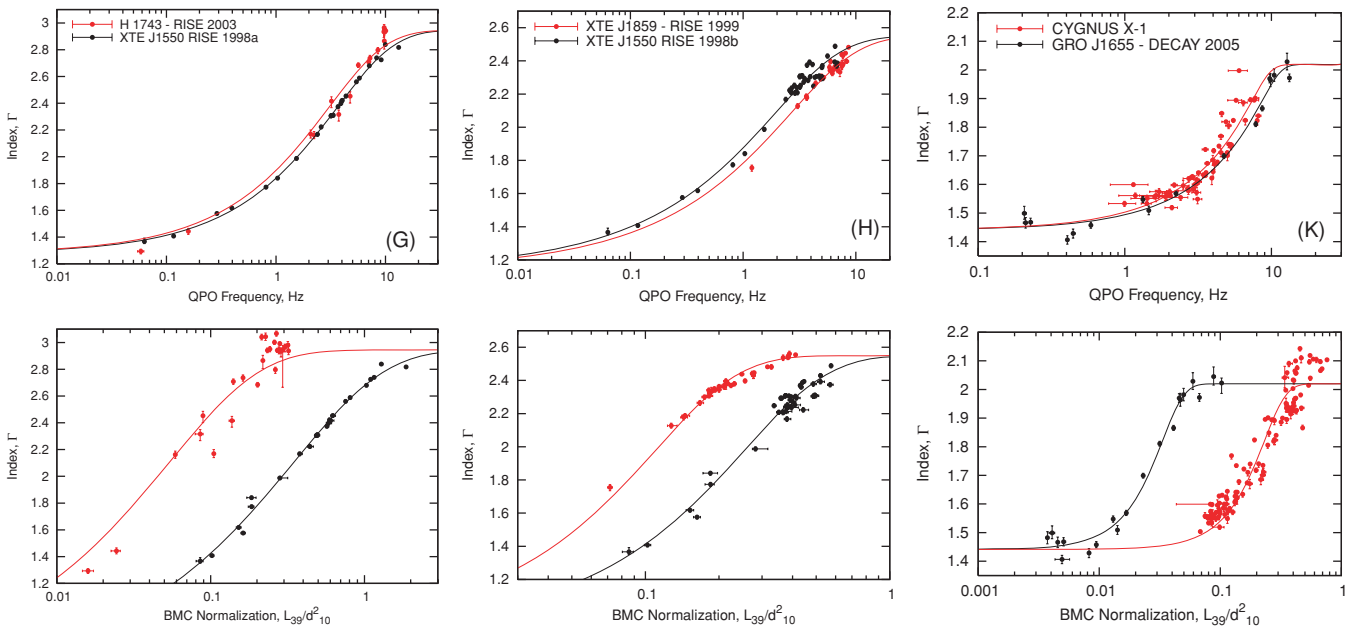

Figure 9. Index–QPO frequency and index–normalization scaling diagrams continued.
(A color version of this figure is available in the online journal.)

Table 5
BH Masses and Distances

Source	$M_{\rm dyn}$[a] ($M_\odot$)	i[a] (deg)	d[b] (kpc)	$M_{\rm ST03}$[c] ($M_\odot$)	$M_{\rm scal}$ ($M_\odot$)	$d_{\rm scal}$ (kpc)	Refs.
GRO J1655−40[d]	6.3 ± 0.3	70 ± 1	3.2 ± 0.2				1, 2
GX 339−4	>6	...	7.5 ± 1.6	9.0 ± 3.8(4)	12.3 ± 1.4	5.75 ± 0.8	5, 6
4U 1543−47	9.4 ± 1.0	20.7 ± 1.5	7.5 ± 1.0	14.8 ± 1.6 (6.4)	9.4 ± 1.4	9.4 ± 1.8	7, 8
XTE J1550−564	9.5 ± 1.1	72 ± 5	∼2.5, ∼6	9.4 ± 2.1 (5)	10.7 ± 1.5	3.3 ± 0.5	9, 10, 11
XTE J1650−500	2.7–7.3	>50	2.6 ± 0.7	10.6 ± 4.0 (5)	9.7 ± 1.6	3.3 ± 0.7	12, 13
H 1743−322	∼11	∼70	∼10	...	13.3 ± 3.2	9.1 ± 1.5	14
XTE J1859−226	7.6–12.0	...	11	12.3 ± 1.7 (11)	7.7 ± 1.3	4.2 ± 0.5	15, 16
Cyg X-1	6.8–13.3	35± 5	2.5 ± 0.3	...	7.9 ± 1.0	2.2 ± 0.3	3, 4

Notes.
[a] Dynamically determined BH mass and system inclination.
[b] Source distances found in the literature.
[c] $M_i = M\cos_i$. Source distances used by ST03 are given in paranthesis.
[d] GRO J1655−40 is a primary reference source. All masses and distances given in Columns 9 and 10 are determined with respect to the best measured parameters for this source.
References. (1) Green et al. 2001; (2) Hjellming & Rupen 1995; (3) Herrero et al. 1995; (4) Ninkov et al. 1987; (5) Muñoz-Darias et al. 2008; (6) Hynes et al. 2004; (7) Orosz 2003; (8) Park et al. 2004; (9) Orosz et al. 2002; (10) Sánchez-Fernández et al. 1999; (11) Sobczak et al. 1999; (12) Orosz et al. 2004; (13) Homan et al. 2006; (14) McClintock et al. 2007; (15) Filippenko & Chornock 2001; (16) Zurita et al. 2002.

several major observational aspects of accreting BHs find natural explanation. We argue that this concept is a strong candidate to provide a basis for a theory of accretion process onto compact objects, which would account for the current observational picture of BH sources. Moreover, this paradigm may provide us with a first direct BH signature observationally confirmed from multiple sources.

The starting point in the development of the TL paradigm is the notion of the necessary deviation of the rotational profile in the innermost part of the disk set by the conditions at (or near) a compact object for which rotation is presumed to be much slower than the Keplerian frequency near the object. This problem was, the first time, considered by TLM98 where the authors showed that the adjustment of the Keplerian rotation in the accretion disk to the sub-Keplerian rotation of the central object leads to the formation of the inner hot CC.

5.1. The Inverse Dependence of the QPO Frequency ν_L on the BH Mass

TLM98 define the TL as a region confined between the inner sub-Keplerian disk boundary (where the inner TL radius $R_{\rm in} = bR_S$, R_S is the Schwarzchild radius and b is a numerical factor $\lesssim 3$) and the first Keplerian orbit (see Figure 1 in TLM98; TF04). Numerical calculations (see also Equation (16) and Figure 2 in TLM98) showed that the value of dimensionless outer radius $r_{\rm out} = R_{\rm out}/R_{\rm in}$ strongly depends on the γ-parameter (Reynolds number) when the rotational velocity of the central of object ω_0 is less than the Keplerian frequency ω_K at the TL outer boundary.

The fact that $r_{\rm out}$ is a function of the γ-parameter implies that the CC dimensionless size $l_{\rm CC} = (R_{\rm out} - R_{\rm in})/R_{\rm in} = r_{\rm out} - 1$ is a function of γ too. Specifically, given that the

γ-parameter defines the spectral state (see TLM98; TL04), the CC dimensionless size $l_{\rm CC}$ is the same for any given spectral state of a BH even if BH masses differ by orders of magnitude. Thus, the CC dimensional size $L_{\rm CC} = bR_{\rm S}l_{\rm CC}(\gamma) \approx 9l_{\rm CC}(\gamma)m$ km is proportional to the BH mass $m = M/M_{\odot}$ for a given spectral state (or γ). Moreover, TLM98 demonstrated that the dimensionless CC size $l_{\rm CC} = L_{\rm CC}/(bR_{\rm S})$ anticorrelates with the X-ray spectral hardness (spectral index). TF04 identified the QPO frequency ν_L as a normal mode oscillation frequency of the CC near the BH. Thus, one should expect that the QPO frequency is inversely proportional to the BH mass given that the QPO frequency is proportional to a ratio of the characteristic velocity with which the perturbation propagates in the CC; note that it is a function of spectral index only, and the CC size $L_{\rm CC} \propto l_{\rm CC}R_{\rm S}$. The CC plasma (sonic or magneto-acoustic) velocity $V_{\rm MA}$ decreases with $\dot{M}$, related to an increase of γ, because in the case of the high mass accretion rate the disk provides strong soft photon illumination of the CC area. In other words, $V_{\rm MA}$ is a strong function of the spectral state (or γ). Given that the QPO frequency ν_L should be expressed as a ratio of $V_{\rm MA}$ to the CC size $L_{\rm CC}$, namely

$$\nu_L \propto \frac{V_{\rm MA}(\gamma)}{L_{\rm CC}(\gamma, m)} \approx \frac{V_{\rm MA}(\gamma)}{9ml_{\rm CC}(\gamma)\rm km}, \quad (11)$$

one can conclude that (1) there should be a correlation of ν_L with the spectral state (or γ) and (2) for a given spectral state, ν_L should be inversely proportional to BH mass m. Thus, if this index–QPO correlation occurring during a spectral transition has a form which is similar to that for another BH source, then there is a possibility to determine a ratio of BH masses for these two BH sources by sliding their correlations along the $\log \nu_L$ axis with respect to each other (see Section 4 for details of an implementation of this scaling technique).

Recent detailed analysis of the spectral and timing properties of X-ray emission in Cyg X-1 by Titarchuk & Shaposhnikov (2008) confirms that the QPO frequency ν_L indeed correlates with the Reynolds number γ and photon index Γ.

The Comptonization Y parameter (or the photon index Γ), which characterizes the efficiency of the Comptonization (see more details in Appendix B), is determined by the product of the average fractional energy change per scattering η and mean number of scattering $N_{\rm sc}$ in the CC. TF04 used the results of the Monte Carlo simulations of Comptonization processes in the CC and the bulk motion flow to demonstrate that Γ increases and then saturates when $\dot{M}$ increases. Thus given that ν_L and Γ correlate with $\dot{M}$, the QPO frequency ν_L should correlate with the photon index Γ as well.

5.2. The Index Saturation Versus Disk Flux as an Observational Evidence of the Converging Flow (Bulk Motion onto a BH)

As we have already pointed out, positive correlations between photon index Γ and QPO frequency should be observed during the state transition, when the corona is cooled down by the disk photons (TLM98; TF04). As the temperature of the CC drops during the transition toward softer states, the BMC effect becomes dominant in the formation of the hard tail of X-ray spectra in BHs in the final spectral stage, that is, in the HSS (see Titarchuk & Zannias 1998, hereafter TZ98, and LT99).

As seen from Figures 2–6, the index saturation is detected in index-*bmc* normalization correlations for most analyzed sources (sometimes the index saturation is seen in the index–QPO correlations too). Namely, the index saturation effect is found in GRO J1655, GX 339, XTE J1550, XTE J1650, H 1743, 4U 1543, Cyg X-1 (see Figures 2–7 and 8 respectively). The saturation level of the index can vary from source to source. Even for the same source, the index saturation can be variable for different transition episodes. For example, GRO J1655−40 exhibits the different index saturation levels $\Gamma_{\rm sat} \sim 2.3$ and 2.05 during the 2005 outburst rise and decay stages, respectively (ST07).

This effect of index saturation versus optical depth of the bulk flow (BM) τ was first predicted by TZ98 and subsequently reproduced in Monte Carlo simulations by LT99. It is worth noting that the index saturation effect is an intrinsic property of the bulk motion onto a BH given that the spectral index $\alpha = \Gamma - 1$ is a reciprocal of the Comptonization parameter Y (see Equation (B7)), which saturates when the BM optical depth τ, or dimensionless mass accretion rate $\dot{m}$, increases. In fact, the Y-parameter is a product of the average fractional photon energy change per scattering η and the mean number of photon scatterings $N_{\rm sc}$, that is, $Y = \eta N_{\rm sc}$.

The thermal Comptonization parameter $Y \sim (4kT/m_ec^2)\tau^2$ given that in this case $\eta = 4kT/m_ec^2$ and $N_{\rm sc} \sim \tau^2$ for $\tau \gg 1$ (see, e.g., Rybicki & Lightman 1979) and, thus, the thermal Comptonization spectral index

$$\alpha \sim [(4kT/m_ec^2)\tau^2]^{-1}. \quad (12)$$

In the case of a converging flow, the preferable direction for upscatterred photons is the direction of bulk motion onto the BH, that is, along its radius. Note that the fractional photon energy change is

$$\Delta E/E = (1 - \mu_1 V_R/c)/(1 - \mu_2 V_R/c),$$

where μ_1 and μ_2 are cosines of angles between the direction of electron velocity $\mathbf{n} = \mathbf{V}_R/V_R$ and directions of incoming and outcoming (scattered) photons respectively.

The number of scattering of up-Comptonized photons $N_{\rm sc}$ can be estimated as a ratio of the radial characteristic size of the converging flow L to the free path l in the direction of motion, namely $N_{\rm sc} \propto L/l = \tau$ given that $\Delta E/E$ has a maximum at $\mu_2 = 1$ for given μ_1 and V_R. On the other hand, the efficiency per scattering for the bulk motion flow $\eta \propto 1/\tau$ when $\tau \gg 1$ (Laurent & Titarchuk 2007).

Thus, one can conclude that the Comptonization parameter $Y = \eta N_{\rm sc}$ and energy index $\alpha = Y^{-1}$ (see Equation (B7)) saturate to a constant value when the optical depth (or mass accretion rate) of the BM flow increases.

The index saturation value is determined by the plasma temperature during a transition (see LT99). On the other hand (see, e.g., TLM98), the plasma temperature strongly depends on the mass accretion rate in the bulk motion region $\dot{M}_{\rm bm}$ and its illumination by the disk photons $F_{\rm disk}$. For higher $\dot{M}_{\rm bm}$ and $F_{\rm disk}$, the plasma temperature is lower. The level of the index saturation decreases when the plasma temperature in the bulk motion increases (TF04). Thus, the index saturation levels can be different from source to source depending on the strength of the disk in a particular case.

6. DISCUSSION

Currently, a BH identification in X-ray observational astronomy is based solely on the mass of a compact object. Namely, a compact X-ray source is classified as a BH if it is well established that its mass exceeds the upper mass limit of a stable rotating neutron star, namely 3.2 $M_{\odot}$ (see, e.g., Rhoades &

Ruffini 1974). To date, there is only one widely accepted method for the mass determination related to the measurement of the mass function $f(M)$ based on optical spectroscopy. While the theoretical mass function is a function of the two masses and the inclination angle, the value of the observationally inferred mass function (which is the minimum possible mass of the compact object) depends only on the velocity half-amplitude K and the orbital period P and independent of the inclination angle i: $f(M) \propto PK^3$.

Orosz (2003) summarized the measurements of the rotational velocities and inclinations for 17 BH binaries. He commented that the difficult part of this procedure has been related to the inverse problem of parameter optimization since the parameter space to search is usually vast and often parameters can be tightly correlated. In many cases, the observed light curve is not entirely due to the companion star owing to the presence of extra sources of light (usually from an accretion disk). Another difficult aspect is the uncertainty in radial velocity amplitude, which appears as third power in a solution. Therefore, while the dynamical mass measurements in a number of BH sources were successful, one should always be cautious about potential systematic errors.

The dynamical measurement of the mass of a compact object of more than the theoretical limit for a stable NS configuration is currently considered a sufficient evidence that the object is a BH. We note, however, that by itself such a mass measurement is not a direct proof of the nature of an object as a BH. Such a proof, for example, would come from the confirmation of the presence of a BH horizon. Direct observations of a BH horizon by theory are not possible. Therefore, one has to look for signatures that would require the BH horizon and therefore would serve as a proof of its presence. In this work, we present theoretical arguments and observational evidence in support that the index saturation effect observed during BH spectral transitions is due to the dynamical Comptonization in the converging bulk motion in the innermost part of a compact object. Formation of this bulk motion region is not possible in the presence of any solid surface, which would otherwise be manifested by observations of a "feed-back" in the form of a strong spectral component due to the energy release on the surface and/or coherent pulsations as in the case of neutron stars. In fact, none of this "feed-back" features was ever observed from these sources. Therefore, we argue that the photon index saturation with the mass accretion rate is the signature of the bulk motion (converging) flow onto a BH. In this paper, we present the observational evidence of the index saturation detected in several X-ray outbursts from BH sources.

We measure the BH mass and distance using scaling relationships in the correlations between spectral and timing properties observed during the state transitions in Galactic accreting BHs. We complement the previously proposed technique for BH mass determination using an index–QPO shift (ST07) by scaling the index−X-ray spectrum normalization, which contains information on a source distance. Using our modified scaling approach, we calculated the BH mass and distances for seven sources. The results of these measurements are given in Table 5. We also present constraints on BH masses and distances, which are available using other methods.

First, we compare the BH masses found using dynamical methods with masses derived by the scaling technique. BH masses provided by scaling are in good agreement with those given by the dynamical method for 4U 1543−47 and XTE J1550−564. For XTE J1859−226 and Cyg X-1, BH mass constraints based on optical measurements are consistent with BH mass values obtained using the scaling technique. A BH mass of $12.3 \pm 1.4\ M_\odot$ obtained for GX 339 is in agreement with the lower limit of $6\ M_\odot$ provided by Muñoz-Darias et al. (2008). For H 1743−322, mass measurement by the dynamical method is not available. Based on the values of high frequency QPOs, McClintock et al. (2007) concluded that H 1743−322 has a high inclination ($i > 70^\circ$) and a BH mass of about 11 solar masses. Our BH mass value of $m = 13.3 \pm 3.2$ agrees with this estimate.

For XTE J1650−500 we obtain a new value for a BH mass of $m = 9.7 \pm 1.6$, which is considerably higher than the upper limit of $7.3\ M_\odot$ inferred by Orosz et al. (2004). In this paper, we also retract our previous claim of the measurement of a BH mass of 3.8 ± 0.5 in XTE J1650−500 (Shaposhnikov & Titarchuk 2008). This preliminary claim for XTE J1650−500 was based on self-similarity of XTE J1650−500 and XTE J1550−564 index–QPO data only. In our study of index correlations with spectrum normalization and other parameters, it has become clear that the data sets used to obtain a low mass value for XTE J1650−500 (J1650−R01 and J1550−98a) are not scalable. The new value of BH mass for XTE J1650−500 is obtained by scaling with GX339−4 using more careful consideration of scalability criteria. It is also worth noting that Orosz et al. (2004) remarked that their analysis were affected by poor statistic and limited number of templates. Moreover, their conclusion on the BH mass upper limit was based on the number of assumptions about the spectral class of the optical companion, accretion disk contribution, and inclination angle.

We hope that future observations will clarify the discrepancy in XTE J1650−500 mass determinations by different methods. We, however, note an interesting fact that most our inferred BH masses, as well as majority of BH masses measured by dynamical methods, fall in a narrow range around $10\ M_\odot$. This may be due to some observational selection effect or some currently unknown factors in stellar evolution. In our opinion, this matter deserves a separate investigation.

In most cases, our distance estimates are also in agreement with distances given by independent methods. A good agreement for 4U 1543−47 and Cyg X-1 is especially encouraging. For these sources, the inclinations are much smaller than that for the reference source GRO J1655−40. This means that an approximation of a geometrical factor $f_{\rm G}$ as a ratio of cosines of inclination angles works well. For H 1743−47, McClintock et al. (2007) inferred an inclination angle of $i \sim 70^\circ$ and a distance of 10 kpc. Using this inferred value of i, we obtained that $f_{\rm G} \sim 1$ and the distance of $d = 9.1 \pm 1.5$ kpc for H 1743−322.

An X-ray spectroscopic method of the BH mass determination was implemented by Borozdin et al. (1999) and further developed in Shrader & Titarchuk (1999). The method is applicable to the HSS data when the thermal BB-like component, which is presumably related to the accretion disk emission, dominates in the emergent X-ray spectrum. The main idea of this X-ray spectroscopic method is to use the color temperature and normalization of the BB component to infer the BH mass. One needs to employ a correct color factor T_h, which is a ratio of the color to the effective BB temperatures of the disk. For the color factor calibration, Borozdin et al. (1999) chose GRO J1655−40 for which d, m, and i are well determined. Analyzing the *RXTE* spectra of this source and using the Shakura–Sunyaev (SS) disk model (Shakura & Sunyaev 1973), they obtained $T_h \sim 2.6$. This is drastically different from the commonly used value of 1.7, obtained by Shimura & Takahara (1995) also in the framework SS

model but with certain assumptions regarding the disk viscosity parameter. Thus, Borozdin et al. (1999) and later Shrader & Titarchuk (1999) used a GRO J1655−40 calibrated value of a color ratio of 2.6 for the BH mass determination. The latest results of the BH mass determination for a number of the black hole candidate (BHC) sources using the X-ray spectroscopy method are summarized in (Shrader & Titarchuk 2003, hereafter ST03). We also present these values in Table 5 for comparison. From this comparison, one may see that the main uncertainties of the ST03 BH mass estimates, which relied on the spectroscopic method, are mostly driven by uncertainties of the inclination i, the distance d, and by the value of the color factor T_h.

7. CONCLUSIONS

We perform a comprehensive study of a highly representative set of well-observed spectral transitions in Galactic BH sources. The goal of the study is to further explore the possibility of measuring the BH fundamental properties from X-ray data and search for BH signatures. We use correlations between spectral and timing properties during the state transitions as a main tool to investigate the BH spectral transition phenomenology.

We compiled the state transition data from eight galactic BH sources collected with the *RXTE* mission. We examine the correlation among the photon index of the Comptonized spectral component, its normalization, and the QPO frequency. By analyzing the behavior of the correlation patterns, we utilize four basic scaling laws: the inverse proportionality of frequencies of oscillatory processes to the mass of a central BH and the disk flux proportionality to the BH mass, mass accretion rate, and its inverse proportionality to a square of distance. We establish that scalable correlation patterns indeed contain information on the BH mass and system distance.

We then combine the scaling of the correlation patterns in the frequency and normalization domains for a set of Galactic X-ray BH binaries from which we determine BH masses and distances. Our results confirm that the correlation scaling method is a powerful technique for a BH mass determination. The application of the scaling technique for the high precision measurements of BH masses requires very well-sampled observations of the source evolution through the outbursts and careful consideration of scalability of correlation patterns.

We have tested the scaling method using the known (from optical, IR observations, and X-ray spectroscopic measurement) BH masses in 4U 1543−47, XTE J1859+226, XTE J1550−564, and Cyg X-1. Using the inverse proportionality of the QPO frequency to a BH mass for a given spectral state we arrive at a set of BH mass determinations, which are in good agreement with available dynamical data for several systems.

We also show observationally that the TL theory (TLM98; TF04) correctly predicts the QPO frequency dependence on the BH mass and overall shape of the correlations between spectral and timing properties observed during spectral transitions. The success of the scaling method for the BH mass determination strongly supports the Compton cloud origin of the observable index–QPO correlation.

We present the observational evidence supporting the theory of the bulk motion (converging) flow, that is, the index saturation with the mass accretion rate. Specifically, by analyzing *RXTE* observations for a set of BH outbursts we find that the index saturation is seen in the index–QPO and index–normalization correlations. We argue that the index saturation with the mass accretion rate as a signature of the bulk (converging) flow should only exist in the BH sources. Only in these sources there is no radiation pressure feedback effect at a high mass accretion rate, as that takes place in NS binaries. In other words, this index saturation effect provides a robust observational evidence of the presence of BHs in these BHCs.

The authors acknowledge the referee for many constructive suggestions to improve the paper quality and its presentation.

APPENDIX A

THE TRANSITION LAYER PARADIGM

The radial motion in the disk is controlled by friction and the angular momentum exchange between adjacent layers, resulting in the loss of the initial angular momentum by accreting matter. The corresponding radial transport of the angular momentum in a disk is described by the following equation (see, e.g., Shakura & Sunyaev 1973):

$$\dot{M}\frac{d}{dR}(\omega R^2) = 2\pi\frac{d}{dR}(W_{r\varphi}R^2), \tag{A1}$$

where $\dot{M}$ is the accretion rate in the disk and $W_{r\varphi}$ is the component of a viscous stress tensor that is related to the gradient of the rotational frequency $\omega = 2\pi\nu$, namely

$$W_{r\varphi} = -2\eta H R\frac{d\omega}{dR}, \tag{A2}$$

where H is the half-thickness of a disk and η is the turbulent viscosity. The nondimensional parameter that is essential for Equation (13) is the Reynolds number for the accretion flow:

$$\gamma = \dot{M}/4\pi\eta H = RV_r/D, \tag{A3}$$

where V_r is the characteristic velocity and D is the diffusion coefficient. D can be defined as $D = V_t l_t/3$ using the turbulent velocity and the related turbulent scale or as $D = D_M = c^2/\sigma$ for the magnetic case, where σ is the conductivity (e.g., see details of the D-definition in Lang 1998).

Equations $\omega = \omega_0$ at $R = R_{\rm in} = bR_{\rm S}$ (at the inner TL radius), $\omega = \omega_K$ at $R = R_{\rm out}$ (the radius where the transition layer adjusts to the Keplerian motion for which $\omega_K = (GM/R^3)^{1/2}$), and $d\omega/dR = d\omega_K/dR$ at $R = R_{\rm out}$ were assumed by TLM98 to be the boundary conditions. Note that here we set the inner boundary at $R_{\rm in} = bR_{\rm S}$ with b of 3. This value of $R_{\rm in}$ is valid for a BH whose spin a is less than 0.8.

Thus, the profile $\omega(R)$ and the outer radius of the transition layer are uniquely determined by the boundary conditions and the angular momentum Equations (A1) and (A2) for a given value of the Reynolds number γ (see Equation (A3)).

The solution of angular momentum Equations (A1) and (A2) satisfying the above boundary conditions is Equation (10) in TLM98 while the following equation (see also Equation (11) in TLM98)

$$3\theta_{\rm out}/2 = D_1\gamma r_{\rm out}^{-\gamma} + 2(1 - D_1)r_{\rm out}^{-2} \tag{A4}$$

determines $r_{\rm out} = R_{\rm out}/R_{\rm in}$ as a function of the γ-parameter. Here, $\theta_{\rm out} = \omega_k(r_{\rm out})/\omega_0$ and $D_1 = (\theta_{\rm out} - r_{\rm out}^{-2})/(r_{\rm out}^{-\gamma} - r_{\rm out}^{-2})$.

The adjustment of the Keplerian disk to the sub-Keplerian inner boundary creates conditions favorable for the formation of a hot plasma outflow at the outer boundary of the transition

layer (TLM98), because the Keplerian motion (if it is followed by sub-Keplerian motion) must pass through a super-Keplerian centrifugal barrier region.

Note that one can see that the right-hand side of Equation (A4) is linearly proportional to $\theta_{\rm out}$ if $\theta_{\rm out} \gg 1$ because $D_1 \propto \theta_{\rm out}$ and $\left|D_1/r_{\rm out}^2\right| \gg 1$ for $\theta_{\rm out} \gg 1$ and $\gamma > 2$. As a result, $\theta_{\rm out}$ can be canceled from left- and right-hand sides of Equation (A4) when $\theta_{\rm out} \gg 1$. Namely, the value of the dimensionless outer radius $r_{\rm out}$ strongly depends on the γ-parameter (Re-number) and independent of $\theta_{\rm out}$ for $\theta_{\rm out} \gg 1$.

It implies that the CC dimensionless size $l_{\rm CC} = (R_{\rm out} - R_{\rm in})/R_{\rm in} = r_{\rm out} - 1$ is a function γ-parameter (Re-number) only if $\theta_{\rm out} \gg 1$. It is worth noting that in the general case, the size $l_{\rm CC}$ is a function of γ and ω_0 (or BH spin a) too. The direct scaling of $L_{\rm CC} = bR_{\rm S}l_{\rm CC}(\gamma, a)$ with the BH mass m is no longer possible. There is a systematic shift of the values of $l_{\rm CC}(\gamma, a)$ for a given γ because of BH spin a.

APPENDIX B

SPECTRAL INDEX α AS A RECIPROCAL OF THE COMPTONIZATION PARAMETER Y

The intensity of the injected soft photons undergoing k scatterings in the Compton cloud is

$$I_k \propto p^k, \tag{B1}$$

where p is a mean probability of photon scattering in the CC. The probability of photon scattering is directly related to the mean number of scatterings:

$$N_{\rm sc} = \sum_{k=1}^{\infty} kp^k q = p/(1-p), \tag{B2}$$

where $q = 1 - p$ is a probability of the photon escape from the CC. Thus, using Equation (B2), we obtain

$$p = 1 - 1/(N_{\rm sc} + 1). \tag{B3}$$

Because the average photon energy change per scattering $\langle \Delta E \rangle = \eta E$ (where $\eta > 0$ for the upscattering case), the injected photon energy after k scatterings E is

$$E = (1+\eta)^k E_0 \tag{B4}$$

The combination of Equations (B1) and (B4) yields that the emergent upscattering spectrum of the soft photon of energy E_0 in the bounded Compton cloud is a power law:

$$I_E \propto \left(\frac{E}{E_0}\right)^{-\alpha}, \tag{B5}$$

whose energy index is

$$\alpha = \frac{\ln(1/p)}{\ln(1+\eta)}. \tag{B6}$$

Using Equation (B3), we can reduce Equation (B6) to

$$\alpha \approx (\eta N_{\rm sc})^{-1} = Y^{-1} \tag{B7}$$

for $N_{\rm sc} \gg 1$ and $\eta \ll 1$.

REFERENCES

Belloni, T. 2005, in AIP Conf. 797, Interacting Binaries: Accretion, Evolution, and Outcomes (New York: AIP), 197
Belloni, T., Homan, J., Casella, P., van der Klis, M., Nespoli, E., Lewin, W. H. G., Miller, J. M., & Méndez, M. 2005, A&A, 440, 207
Belloni, T., et al. 2006, MNRAS, 367, 1113
Borozdin, K., Revnivtsev, M., Trudolyubov, S., Shrader, C., & Titarchuk, L. 1999, ApJ, 517, 367
Casella, P., Belloni, T., Homan, J., & Stella, L. 2004, A&A, 426, 587
Dewangan, G. C., Titarchuk, L., & Griffiths, R. E. 2006, ApJ, 637, L21
Dickey, J. M., & Lockman, F. J. 1990, ARA&A, 28, 215
Filippenko, A. V., & Chornock, R. 2001, IAU Circ., 7644, 2
Fiorito, R., & Titarchuk, L. 2004, ApJ, 614, L113
Greene, J., Bailyn, C. D., & Orosz, J. A. 2001, ApJ, 554, 1290
Herrero, J., et al. 1995, A&A, 297, 556
Hjellming, R. M., & Rupen, M. P. 1995, Nature, 375, 464
Homan, J., Wijnands, R., Kong, A., Miller, J. M., Rossi, S., Belloni, T., & Lewin, W. H. G. 2006, MNRAS, 366, 235
Hynes, R. I., Steeghs, D., Casares, J., Charles, P. A., & O'Brien, K. 2004, ApJ, 609, 317
Kalemci, E., Tomsick, J. A., Buxton, M. M., Rothschild, R. E., Pottschmidt, K., Corbel, S., Brocksopp, C., & Kaaret, P. 2005, ApJ, 622, 508
Klein-Wolt, M., & van der Klis, M. 2008, ApJ, 675, 1407
Lang, K. R. 1998, Astrophysical Formulae (Berlin: Springer)
Laurent, P., & Titarchuk, L. 1999, ApJ, 511, 289 (LT99)
Laurent, P., & Titarchuk, L. 2007, ApJ, 656, 1056
McClintock, J. E., Remillard, R. A., Rupen, M. P., Torres, M. A. P., Steeghs, D., Levine, A. M., & Orosz, J. A. 2007, arXiv:0705.1034
Montanari, E., Titarchuk, L., & Frontera, F. 2009, ApJ, 692, 1597
Muñoz-Darias, T., Casares, J., & Martínez-Pais, I. G. 2008, MNRAS, 385, 2205
Ninkov, Z., Walker, G. A. H., & Yang, S. 1987, ApJ, 321, 425
Orosz, J. A. 2003, in IAU Symp. 212, A Massive Star Odyssey: From Main Sequence to Supernova, ed. K. van der Hucht, A. Herrero, & E. César (San Francisco, CA: ASP), 365
Orosz, J. A., McClintock, J. E., Remillard, R. A., & Corbel, S. 2004, ApJ, 616, 376
Orosz, J. A., et al. 2002, ApJ, 568, 845
Park, S. Q., et al. 2004, ApJ, 610, 378
Remillard, R. A., & McClintock, J. E. 2006, ARA&A, 44, 49
Revnivtsev, M., Gilfanov, M., & Churazov, E. 2000, A&A, 363, 1013
Rhoades, C. E. Jr., & Ruffini, R. 1974, Phys. Rev. Lett., 32, 324
Rodriguez, J., Corbel, S., Kalemci, E., Tomsick, J. A., & Tagger, M. 2004, ApJ, 612, 1018
Rodriguez, J., Corbel, S., & Tomsick, J. A. 2003, ApJ, 595, 1032
Rossi, S., Homan, J., Miller, J. M., & Belloni, T. 2004, Nucl. Phys. B, 132, 416
Rybicki, G. B., & Lightman, A. P. 1979, Radiative Processes in Astrophysics (New York: Wiley Interscience)
Sánchez-Fernández, C., et al. 1999, A&A, 348, L9
Shakura, N. I., & Sunyaev, R. A. 1973, A&A, 24, 337
Shaposhnikov, N., & Titarchuk, L. 2006, ApJ, 643, 1098 (ST06)
Shaposhnikov, N., & Titarchuk, L. 2007, ApJ, 663, 445 (ST07)
Shaposhnikov, N., & Titarchuk, L. 2008, AAS/High Energy Astrophysics Division, 10, 01.08
Shimura, T., & Takahara, F. 1995, ApJ, 445, 780
Shrader, C., & Titarchuk, L. G. 2003, ApJ, 598, 168
Shrader, C., & Titarchuk, L. G. 1999, ApJ, 521, L121
Sobczak, G. J., McClintock, J. E., Remillard, R. A., Levine, A. M., Morgan, E. H., Bailyn, C. D., & Orosz, J. A. 1999, ApJ, 517, L121
Strohmayer, T. E., Mushotzky, R, Winter, L., Soria, R., Uttley, P., & Cropper, M. 2007, ApJ, in press (arXiv:astro-ph/0701390)
Sunyaev, R. A., & Titarchuk, L. G. 1980, A&A, 86, 121
Titarchuk, L., Lapidus, I. I., & Muslimov, A. 1998, ApJ, 499, 315 (TLM98)
Titarchuk, L., Mastichiadis, A., & Kylafis, N. D. 1997, ApJ, 487, 834
Titarchuk, L., & Shaposhnikov, N. 2008, ApJ, 678, 1230
Titarchuk, L., & Zannias, T. 1998, ApJ, 493, 863
Titarchuk, L. G., & Fiorito, R. 2004, ApJ, 612, 988 (TF04)
Trudolyubov, S. P. 2001, ApJ, 558, 276
Trudolyubov, S. P., Borozdin, K. N., & Priedhorsky, W. C. 2001, MNRAS, 322, 309
Vignarca, F., Migliari, S., Belloni, T., Psaltis, D., & van der Klis, M. 2003, A&A, 397, 729
Zurita, C., et al. 2002, MNRAS, 334, 999